DispatchDate: 22.11.2021 · ProofNo: 142, p.1

nature aging

LETTERS

https://doi.org/10.1038/s43587-021-00142-3

Check for updates

Profiling senescent cells in human brains reveals neurons with CDKN2D/p19 and tau neuropathology

Shiva Kazempour Dehkordi[1,2,14], Jamie Walker[1,14], Eric Sah[3], Emma Bennett[3], Farzaneh Atrian[2,4], Bess Frost[1,2,4], Benjamin Woost[5], Rachel E. Bennett[5], Timothy C. Orr[6], Yingyue Zhou[7], Prabhakar S. Andhey[7], Marco Colonna[7], Peter H. Sudmant[8], Peng Xu[9,10,11], Minghui Wang[9,10,11], Bin Zhang[9,10,11,12], Habil Zare[1,2] ✉ and Miranda E. Orr[3,13] ✉

Senescent cells contribute to pathology and dysfunction in animal models[1]. Their sparse distribution and heterogenous phenotype have presented challenges to their detection in human tissues. We developed a senescence eigengene approach to identify these rare cells within large, diverse populations of postmortem human brain cells. Eigengenes are useful when no single gene reliably captures a phenotype, for example, senescence; they also help to reduce noise, which is important in large transcriptomic datasets where subtle signals from low-expressing genes can be lost. Each of our eigengenes detected around 2% senescent cells from a population of around 140,000 single nuclei derived from 76 postmortem human brains with various levels of Alzheimer's disease (AD) pathology. More than 97% of the senescent cells were excitatory neurons and overlapped with tau-containing neurofibrillary tangles (NFTs). Cyclin-dependent kinase inhibitor 2D (*CDKN2D*/p19) was predicted as the most significant contributor to the primary senescence eigengene. RNAscope and immunofluorescence confirmed its elevated expression in AD brain tissue, whereby p19-expressing neurons had 1.8-fold larger nuclei and significantly more cells with lipofuscin than p19-negative neurons. These hallmark senescence phenotypes were further elevated in the presence of NFTs. Collectively, *CDKN2D*/p19-expressing neurons with NFTs represent a unique cellular population in human AD with a senescence phenotype. The eigengenes developed may be useful in future senescence profiling studies as they identified senescent cells accurately in snRNA-Seq datasets and predicted biomarkers for histological investigation.

Cellular senescence is a complex stress response that culminates as a change in cell fate. Senescent cells are cell cycle arrested and resistant to apoptosis[1]. Their survival contributes to long-term health decline as, notoriously, they secrete a molecular milieu, referred to as senescence-associated secretory phenotype (SASP), that negatively impacts their extracellular environment[2]. Data from rodent models indicate that senescent neurons[3–6], astrocytes[7], microglia[8] and oligodendrocyte precursor cells[9] contribute to neurodegeneration and cognitive dysfunction. Information on the relative proportion of senescent cells in humans has been restricted to accessible tissues (~2–5% in skin, adipose and blood[10,11]). Identifying senescent cells in human AD presents challenges beyond their low abundance and the inability to routinely biopsy brain tissue. For example, in-vitro-based molecular profiles and senescence assays generate inconsistent results when applied to the brain, p16 and/or p21 senescence marker genes signify aberrant neuronal cycle activity and are upregulated during cell differentiation and glial activation independent of senescence[12–14], and brain cells secrete molecules that overlap with SASP factors in the absence of a cell cycle arrest (that is, glial cells become hyperproliferative and inflammatory in many neurodegenerative diseases[15,16]). To overcome these obstacles, we developed unbiased bioinformatic tools—senescence eigengenes—to identify and profile senescent cells in human AD.

We created three eigengenes representing distinct features of senescence—stress response, cell cycle arrest and inflammatory response—to minimize the likelihood of mistaking cells with one, but not all, key senescent phenotypes. Thus, senescent cells could be distinguished from those that may be cell cycle arrested, stressed or inflammatory, independent of senescence. Each eigengene included genes commonly associated with senescence that had been reported across cell and tissue types, including those from aged and transgenic mouse models of AD pathology[3–9]. The gene sets reflected (1) a canonical senescence pathway (CSP) with 22 genes including *CDKN2A* and *CDKN1A* that are upregulated in many senescent cell types; (2) 48 genes upregulated early in senescence, which we termed senescence initiating pathway (SIP) and (3) 44 genes upregulated after the stable arrest and involved in SASP production, which

[1]Glenn Biggs Institute for Alzheimer's and Neurodegenerative Diseases, San Antonio, TX, USA. [2]Department of Cell Systems and Anatomy, University of Texas Health San Antonio, San Antonio, TX, USA. [3]Department of Internal Medicine, Wake Forest School of Medicine, Winston-Salem, NC, USA. [4]Sam and Ann Barshop Institute for Longevity and Aging Studies, University of Texas Health San Antonio, San Antonio, TX, USA. [5]Department of Neurology, MassGeneral Institute for Neurodegenerative Disease, Massachusetts General Hospital, Harvard Medical School, Charlestown, MA, USA. [6]Department of Healthcare Innovations, Wake Forest School of Medicine, Winston-Salem, NC, USA. [7]Department of Pathology and Immunology, Washington University School of Medicine, St. Louis, MO, USA. [8]Department of Integrative Biology, University of California Berkeley, Berkeley, CA, USA. [9]Department of Genetics and Genomic Sciences, Icahn School of Medicine at Mount Sinai, One Gustave L. Levy Place, New York, NY, USA. [10]Mount Sinai Center for Transformative Disease Modeling, Icahn School of Medicine at Mount Sinai, One Gustave L. Levy Place, New York, NY, USA. [11]Icahn Institute for Data Science and Genomic Technology, Icahn School of Medicine at Mount Sinai, One Gustave L. Levy Place, New York, NY, USA. [12]Department of Department of Pharmacological Sciences, Icahn School of Medicine at Mount Sinai, One Gustave L. Levy Place, New York, NY, USA. [13]Salisbury VA Medical Center, Salisbury, NC, USA. [14]These authors contributed equally: Shiva Kazempour Dehkordi, Jamie Walker. ✉e-mail: zare@uthscsa.edu; morr@wakehealth.edu

we termed senescence response pathway (SRP) (Supplementary Table 1). For each of these three gene sets, we performed a principal component analysis to compute a weighted average expression over all genes in the corresponding list[17], that is, an eigengene[18]. Weights were optimized in such a way that explained variance was maximized and, thus, the loss of biological information is expected to be minimal. Cells were considered to be senescent if their level of eigengene expression was more than the mean expression over all cells plus three times the s.d. (mean + 3 s.d.).

Two independent single-nucleus RNA sequencing (snRNA-Seq) datasets were used[19,20], referred to as cohort 1 and cohort 2, respectively. Analyses using the CSP eigengene revealed 1,526 senescent cells in the dorsolateral prefrontal cortex (2.1%) from cohort 1; the proportion differed across individuals (0–13%, Fig. 1a–g). A total of 1,351 cells and 1,256 cells expressed the SIP and SRP, respectively (2% and 1.7%, Fig. 1a–c). Similar results were derived from cohort 2, whereby 1,331 (2.3%), 1,485 (2.6%) and 951 (1.6%) cells expressed the CSP, SIP and SRP eigengenes, respectively (Supplementary Fig. 1 and Supplementary Table 2). We used a dataset generated from embryonic brains as a control[21]; notably, the eigengenes identified few senescent cells (CSP: 16 (0.4%); SIP: 23 (0.6%); SRP: 82 (2%), Extended Data Fig. 1).

To determine which brain cell type(s) were overrepresented in the senescent cell population, we used a hypergeometric test to categorize the overlap with cell types, as defined in the original studies[19,20]. In cohort 1, excitatory neurons were the only cell population with more than expected senescent cells based on all three senescence gene sets (Fig. 1d–g). Subpopulations of astrocytes, endothelial cells and pericytes expressed gene patterns consistent with inflammation (SRP) but not with canonical senescence. Cohort 2 produced similar results, where the number of cells expressing CSP and SIP eigengenes were overrepresented in excitatory neurons. Astrocytes and endothelial cells were identified to express the SRP eigengene, which may reflect an inflammatory phenotype independent of a canonical senescence stress response[22,23] (Extended Data Fig. 2). Endothelial cells were also identified based on the CSP eigengene, but only in cohort 2. These data may indicate vascular cell senescence in the brain, as seen in cardiovascular disease[24], and recently reported in human AD[22]. Similarly, in the embryonic dataset, the higher expression of SRP reflected endothelial cells, 77 (49%). However, they did not express either the CSP or SIP eigengenes, indicating an incomplete senescence profile that may reflect physiological senescence or developmental processes associated with these molecules[25,26]. Excluding endothelial cells, the number of identified senescent cells in the embryonic brains was significantly fewer than the rate of around 2% in cohorts 1 and 2 ($-\log_{10} P$ values from binomial tests: 16 for CSP, 12 for SIP and 26 for SRP). Collectively, the predominant senescent cell population in both adult brain cohorts was excitatory neurons, representing 97% and 92% of CSP cells in cohort 1 and cohort 2, respectively. Even in the dataset of Grubman et al.[27], in which neurons were undersampled due to use of single-cell (sc) profiling (that is, only 656 (5%) neurons were sequenced), neurons had the highest rate, and the most significant P value, of CSP senescent enrichment (Supplementary Fig. 2).

The relative proportion of senescent excitatory neurons to total excitatory neurons within individual brains varied among individuals and ranged from 0% to 20%. On average, 4.2%, 3.5% and 2.5% excitatory neurons in cohort 1 were senescent as determined using the CSP, SIP and SRP eigengenes, respectively ($-\log_{10} P$ value: 3,143, 2,027 and 380, respectively, Fig. 1h–j); Cohort 2, Supplementary Fig. 1. Moreover, the senescent cells identified based on these three eigengenes overlapped significantly ($-\log_{10} P$ value: >232, Extended Data Fig. 3). There was no significant association between the number of excitatory neurons expressing CSP, SIP and SRP eigengenes with sex (P values: >0.7, >0.7 and >0.6, respectively) or age (P values: >0.5, >0.2 and >0.3, respectively). In relation to cohort 1, brains from cohort 2 had similar senescent cell burden and between-subject variability (Supplementary Fig. 1) but a higher proportion of excitatory neurons expressing CSP and SIP (9.7% and 10.3%, respectively) with <1% expressing SRP ($-\log_{10} P$ values: 4,820, 4,663 and 0, respectively; Extended Data Fig. 2 and Supplementary Fig. 3).

As described above, the three CSP, SIP and SRP eigengenes were designed to capture distinct aspects of senescence that we reasoned would be associated in senescent cells, but not necessarily associated in nonsenescent cells. To test this hypothesis, we evaluated the correlation among the three senescence eigengenes within excitatory neurons. The ratio of senescent excitatory neurons, as defined by CSP, correlated highly with SIP (Pearson correlation: 0.96) and SRP (0.90). Moreover, brains with higher proportions of senescent neurons displayed higher eigengene expression levels (Fig. 1k). Pathways were similarly correlated in cohort 2 (CSP and SIP: 0.94, Supplementary Fig. 3). Thus, the eigengenes were significantly associated, and excitatory neurons represented the predominant senescent cell type across the ~140,000 cells analyzed in these 76 brains as determined by three independent eigengenes (that is, signatures) of senescence.

To confirm that these results were not an artifact of our gene lists, we computed an eigengene for senescence per each of the gene lists obtained from CellAge[28], Gene Ontology (GO)[29,30] and Kyoto Encyclopedia of Genes and Genomes (KEGG)[31] databases (Supplementary Table 1). These eigengenes showed that 3.5%, 3.7% and 3.4% excitatory neurons in cohort 1 were senescent, respectively, which is significantly more than expected by chance ($-\log_{10} P$ value: 2,534, 2,673 and 2,277, respectively; Extended Data Fig. 4). Overall, the overlap between the identified senescent cells based on the six CSP, SIP, SRP, CellAge, GO and KEGG eigengenes was significantly more than expected by chance ($-\log_{10} P$ value >232; Extended Data Fig. 5).

The accumulation of intraneuronal tau protein is a common pathology across neurodegenerative diseases including AD[32]. NFTs are characterized histologically by the presence of aggregated, phosphorylated misfolded tau proteins. They accumulate preferentially in excitatory neurons in human AD[33] and drive senescence in transgenic mice[3,8]. We hypothesized that excitatory neurons containing NFTs may be a source of senescent excitatory neurons detected by the eigengenes. To quantify the association between NFTs and senescence, we created eigengenes from two independent gene lists derived from laser capture microdissected neurons with NFTs[34,35], referred to as 'NFT$^{\text{Duckley}}$' and 'NFT$^{\text{Garcia}}$', respectively. Using the NFT eigengenes, we identified 1,050 NFT$^{\text{Dunckley}}$ cells and 1,022 NFT$^{\text{Garcia}}$ cells in cohort 1, reflecting 1.5% and 1.4% of the total cellular population, respectively (Fig. 2). The overlap between NFT$^{\text{Dunckley}}$ cells and NFT$^{\text{Garcia}}$ cells was significant (that is, 765 (1%) cells, $-\log_{10} P$ value: 3,035). Cohort 2 had slightly higher levels of NFT-bearing neurons than cohort 1, specifically 1,523 (2.6%) NFT$^{\text{Dunckley}}$ and 1,761 (3%) NFT$^{\text{Garcia}}$ cells with a significant overlap of 1,214 (2%) cells ($-\log_{10} P$ value: 4,038; Supplementary Fig. 4). As expected, we did not identify any NFT$^{\text{Dunckley}}$ or NFT$^{\text{Garcia}}$ cells in the embryonic control brains (Supplementary Table 2). In both cohorts 1 and 2, and based on both NFT$^{\text{Dunckley}}$ and NFT$^{\text{Garcia}}$ eigengenes, the predominant cell type expressing the NFT eigengenes was excitatory neurons. These data are consistent with NFTs driving neuronal senescence in transgenic mice[3] and preferential accumulation in excitatory neurons in AD[33].

As observed with senescence, the relative proportion of NFT-containing neurons to all excitatory neurons varied across individuals in cohort 1 (Fig. 2d,e) and cohort 2 (Supplementary Fig. 5). Since the cell type (that is, excitatory neurons) and proportions were consistent with other reports[33,36], we interpreted that the eigengene could be used as a transcriptional surrogate to identify NFT-bearing neurons. Plotting NFT eigengene expression against senescence eigengene expression revealed a significant relationship

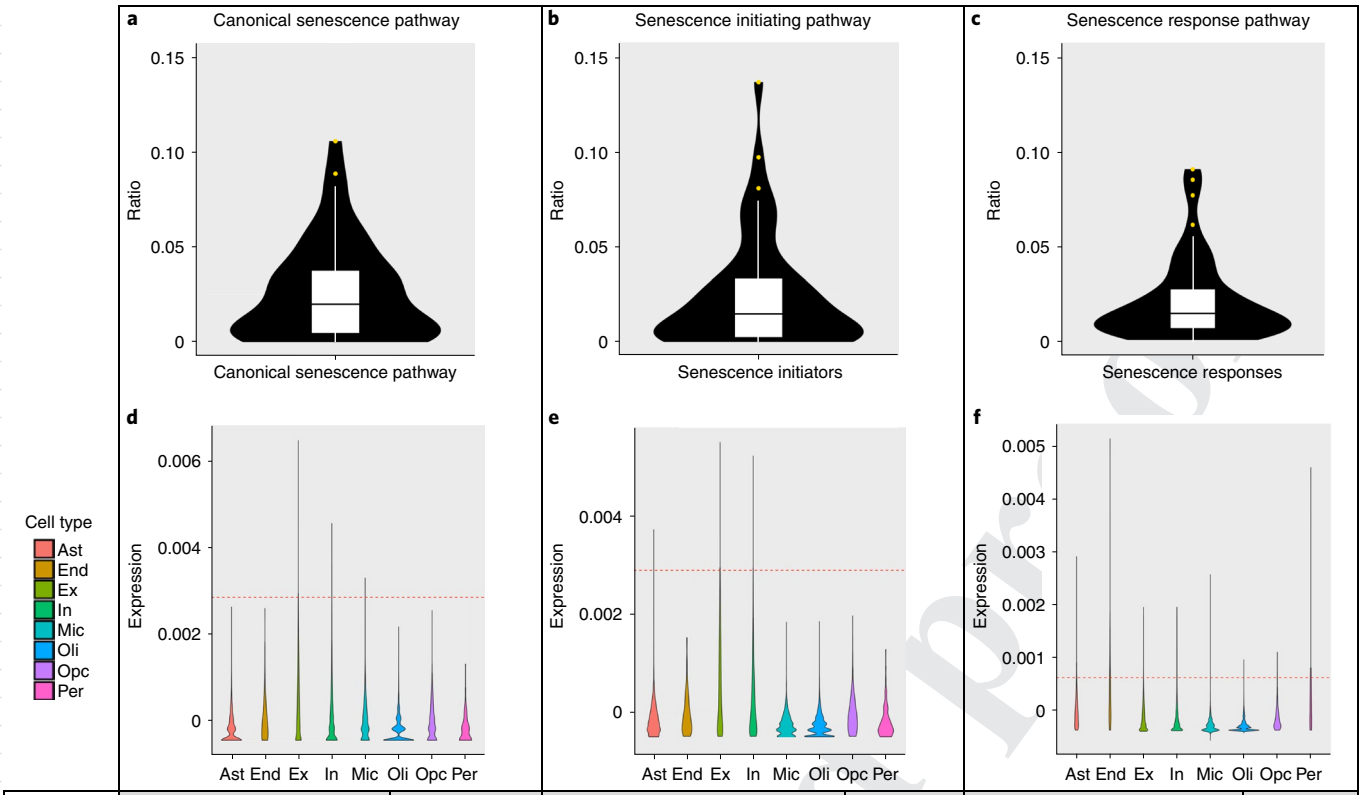

g

Cell types	Cell numbers		$\log_{10}(P$ value)	Cell numbers		$\log_{10}(P$ value)	Cell numbers		$\log_{10}(P$ value)
	Normal	Senescent		Normal	Senescent		Normal	Senescent	
Ast	3,392	0	0	3,391	1	~0	3,224	168	–258
End	121	0	0	121	0	0	87	34	–241
Ex	33,491	1,485	–3130	33,734	1,242	–2019	34,102	874	-377
In	9,156	40	~0	9,088	108	~0	9,079	108	~0
Mic	1,919	1	~0	1,920	0	0	1,917	3	~0
Oli	18,235	0	0	18,235	0	0	18,232	3	~0
Opc	2,627	0	0	2,627	0	0	2,612	15	~0
Per	167	0	0	167	0	0	125	42	–279

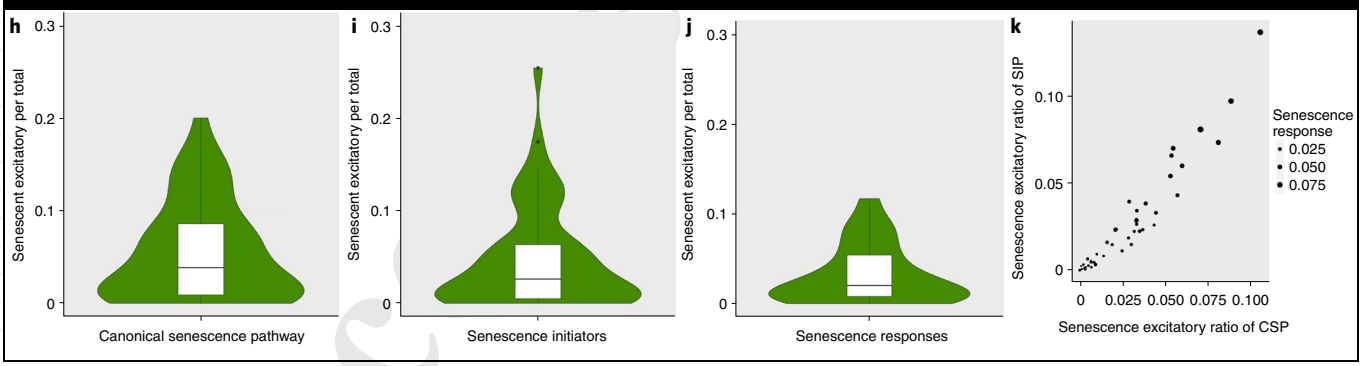

Fig. 1 | The prominent senescent cell type in the dorsolateral prefrontal cortex were excitatory neurons. a–j, Eigengenes for each gene list using $n = 70{,}634$ cells in CSP (**a**,**d**,**h**), SIP (**b**,**e**,**i**) and SRP (**c**,**f**,**j**) were computed using principal component analyses. The proportion of cells from each brain expressing the respective eigengene were plotted (**a–c**). Cell types (**d–f**) and counts (**g**) represented in the senescent cell population discovered in **a–c** are shown. A one-sided hypergeometric test was used to report the significant cell types. All the *P* values were adjusted using Bonferroni correction. The ratio of senescent excitatory neurons that expressed the respective eigengenes to total neurons within each brain is shown (**h–j**), $n = 48$ brains. **k**, Scatter plot for the ratio of senescent excitatory neurons to the total number of excitatory neurons in cohort 1 with $n = 48$ brains. Each dot represents one brain. The size of the dots depicts the ratio in SRP. The senescence excitatory ratios of CSP correlated highly with SIP (Pearson correlation: 0.96) and SRP (0.90). Also, the SIP ratio was correlated positively with the SRP ratio (0.93). The line inside each box plot in **a–c** and **h–j** shows the median. The lower and upper hinges of box plots correspond to the first and the third quartiles, respectively. The whiskers extend from the bottom or the top of the box for, at most, 1.5 of the interquartile range, which is the distance between first and third quartiles. Samples not between the whiskers were considered outliers, which are shown with yellow (**a–c**) and black (**h–j**) dots. Cell populations: astrocytes (Ast), endothelial cells (End), excitatory neurons (Ex), inhibitory neuron (In), microglia (Mic), oligodendrocytes (Oli), oligodendrocyte precursor cells (Opc) and pericytes (Per) were classified in the original publication[21].

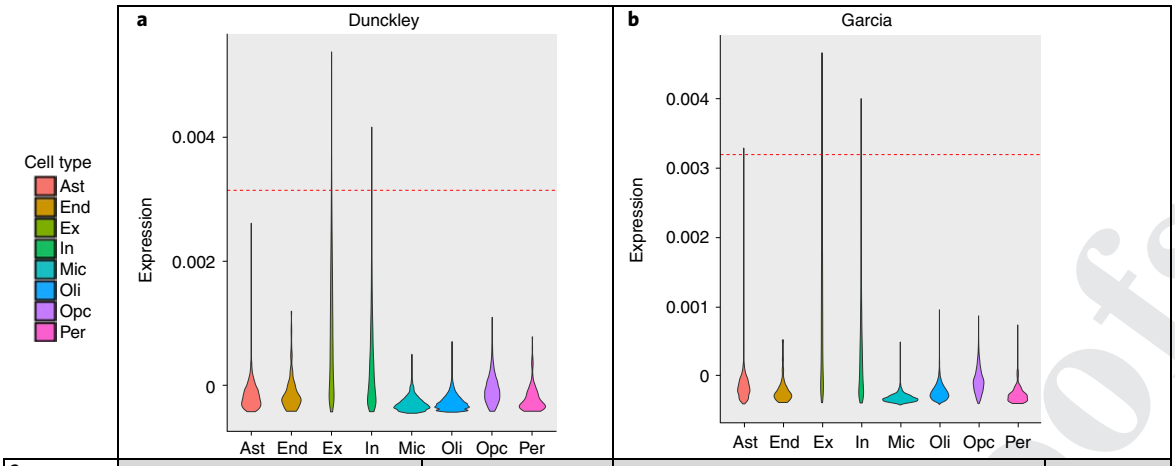

c Cell types	Cell numbers		$\log_{10}(P$ value)	Cell numbers		$\log_{10}(P$ value)
	Normal	NFT		Normal	NFT	
Ast	3,392	0	0	3,391	1	~0
End	121	0	0	121	0	0
Ex	33,944	1,032	−2,280	33,968	1,008	−2,270
In	9,178	18	~0	9,183	13	~0
Mic	1,920	0	0	1,920	0	0
Oli	18,235	0	0	18,235	0	0
Opc	2,627	0	0	2,627	0	0
Per	167	0	0	167	0	0

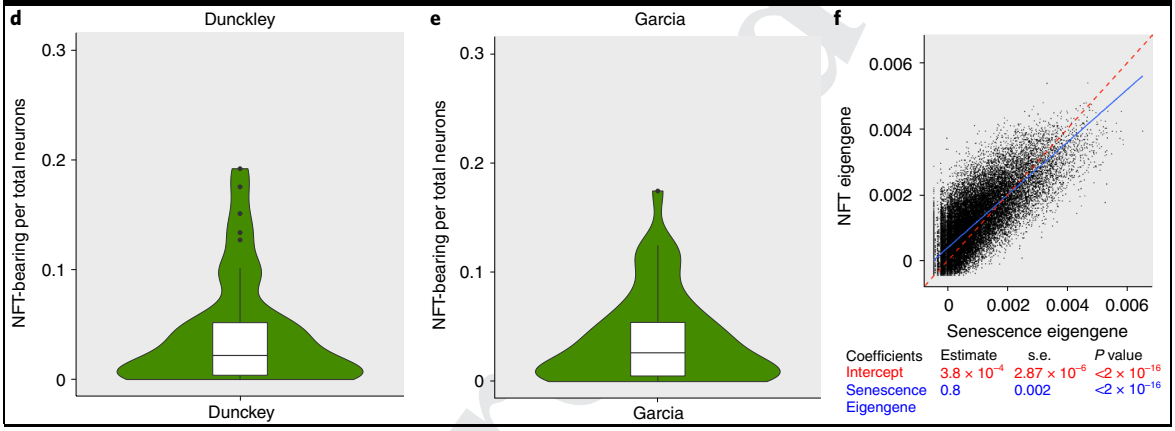

Fig. 2 | NFT eigengene expression correlated significantly with senescence expression. a,**b**, Eigengenes representing NFT expression were calculated from two separate datasets: Dunckley[34] and Garcia[35]. Cell types (**a**,**b**) and counts (**c**) expressing each NFT eigengene were calculated and plotted using $n = 70{,}634$ cells. A one-sided hypergeometric test was used to report the significant cell types. All *P* values were adjusted using Bonferroni correction. **d**,**e**, The ratio of NFT-containing excitatory (Ex) neurons to total neurons expressing each respective eigengene within each brain, $n = 48$ brains; the line inside each box plot shows the median. The lower and upper hinges of box plots correspond to the first and the third quartiles, respectively. The whiskers extend from the bottom or the top of the box for at most 1.5 of the interquartile range. Any sample not between the whiskers is known as an outlier and is shown with a black dot. **f**, Scatter plot for eigengene values for CSP genes on the *x* axis versus Dunckley NFT marker genes on the *y* axis. Each dot represents one neuron. The red line represents the intercept, and the blue line shows the best linear fit. A linear regression model is fitted on NFT ~ Senescence with coefficient being equal to zero as the null hypothesis.

between them ($-\log_{10} P$ value >15, adjusted $R^2 = 0.6803$, m = 0.863, Fig. 2f). Hypergeometric tests were used to assess the association between senescent and NFT-bearing cells. In cohort 1, we identified 1,485 CSP senescent excitatory neurons and 1,032 $NFT^{Dunckley}$-bearing excitatory neurons. We expected to identify 44 overlapping cells if senescence and NFTs were not associated (that is, coexpression by chance); however, 598 cells coexpressed both eigengenes, indicating a significant association ($-\log_{10}$ adjusted *P* value = 1,337; Supplementary Table 3). Similar results were obtained in cohort 2 and using the NFT^{Garcia} eigengene (Supplementary Table 3). $NFT^{Dunckley}$-bearing excitatory neurons also significantly overlapped with SIP and SRP senescent cells ($-\log_{10} P$ values >231; Extended Data Fig. 3). These data confirmed the significant association whereby the senescence and NFT eigengenes were upregulated within the same cells.

Senescent and NFT neurons constituted a minor proportion of all neurons (that is, of the 44,172 total neurons analyzed in cohort 1, only 3.4% and 2.3% excitatory neurons met the criteria of senescent and NFTs, respectively). To visualize overlap between senescent and NFT neuron populations, we plotted their distributions within the entire neuronal population. These data revealed a continuum of senescence gene expression whereby 99% of NFT-bearing neurons displayed upregulated senescence eigengene greater than that of neurons without NFTs (Fig. 3). Specifically, the density plots

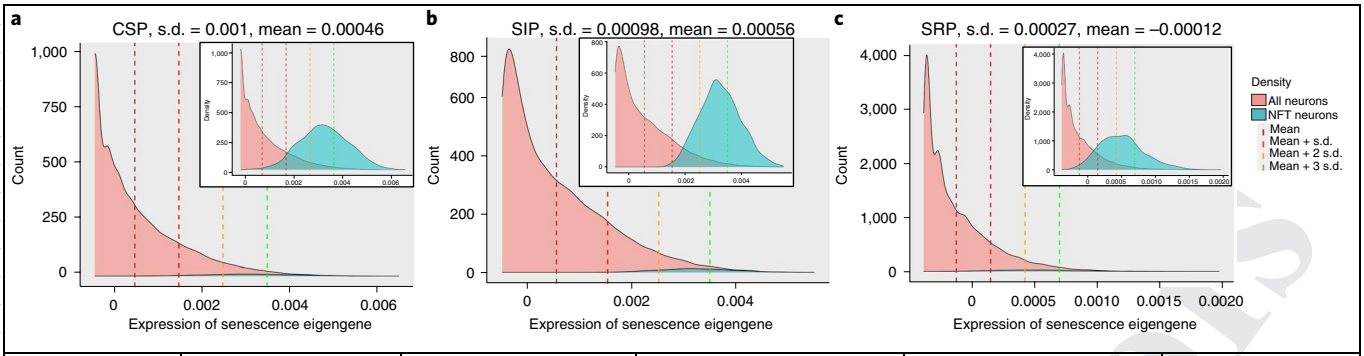

NFT neurons n = 1,050	No. of nonsenescent NFT < mean	Mean< No. of senescent NFT < mean + s.d.	Mean + s.d. < No. of senescent NFT < mean + 2 s.d.	Mean + 2 s.d. < No. of senescent NFT < mean + 3 s.d.	No. of senescent NFT > mean + 3 s.d.
CSP	5 (<1%)	46 (4.38%)	244 (23.24%)	393 (37.43%)	362 (34.48%)
SIP	0 (0%)	4 (<1%)	169 (16.10%)	513 (48.86%)	364 (34.67%)
CRP	12 (1.14%)	127 (12.10%)	319 (30.38%)	321 (30.57%)	271 (25.81%)

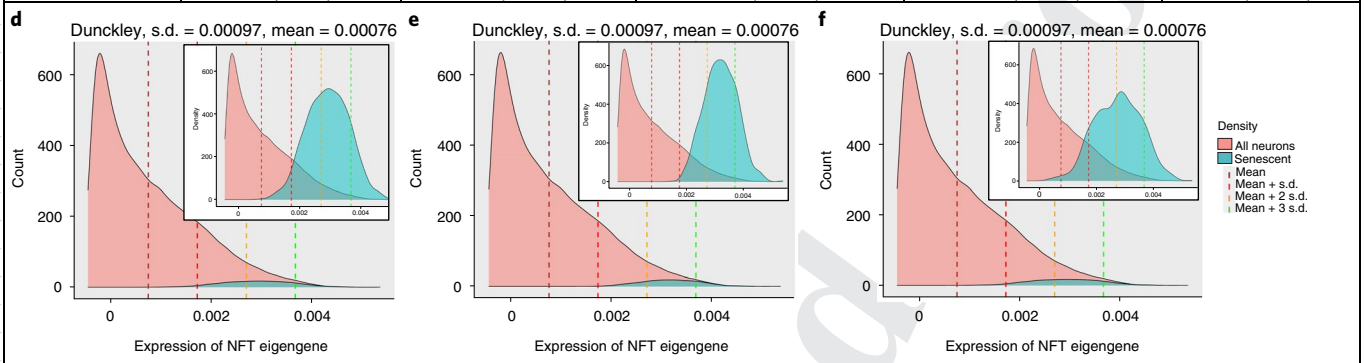

Senescent pathway	No. of non-NFT senescent < mean	Mean < No. of NFT senescent < mean + s.d.	Mean + s.d. < No. of NFT senescent < mean + 2 s.d.	Mean + 2 s.d. < No. of NFT senescent < mean + 3 s.d.	No. of NFT senescent >mean + 3 s.d.
CSP: 1,525	0 (0%)	59 (3.87%)	524 (34.36%)	735 (48.20%)	206 (13.51%)
SIP: 1,350	0 (0%)	1 (<1%)	288 (21.33%)	792 (58.67%)	269 (19.93%)
SRP: 991	8 (<1%)	104 (10.49%)	345 (34.81%)	402 (40.57%)	132 (13.32%)

Fig. 3 | Senescent excitatory neurons contain NFTs, and NFT-bearing neurons are senescent. a–c, Plots of total neuron counts (pink) against expression of the eigengene CSP, SIP or SRP. Cell densities of where NFT-bearing neurons (green) lie within the plot are shown (insets). **d–f**, Plots of total neuron counts (pink) against expression of the NFT^{Dunckley} eigengene. Cell densities of where CSP, SRP or SIP cell populations lie within the plot are shown (insets). Larger plots are scaled by the number of cells and insets are scaled by cell density. Mean and s.d. are calculated for the eigengene value of all neurons.

indicated that <1% of NFT-bearing neurons expressed the CSP eigengene lower than the mean (that is, <1% of neurons with NFTs could be confidently considered not senescent, Fig. 3a). However, we are cautious not to label the remaining 99% of NFT-bearing neurons as senescent. Our stringent cutoff required expression levels greater than mean + 3 s.d. With these criteria, 35% of NFT-bearing neurons were identified as senescent and <1% as not senescent. The remaining 64% of NFT-bearing neurons could not be considered either senescent or not senescent, but instead showing upregulated senescence eigengene expression. Similar patterns were observed across all eigengenes to confirm and validate the interpretation (Fig. 3a–c). We also determined the distribution of the senescent neurons identified to contain NFTs (that is, used the same experimental approach, but asked the question in the opposite direction). In cohort 1, all senescent cells expressed the NFT eigengene greater than the mean of all neurons (Fig. 3d–f). Approximately 14% of the senescent neurons coexpressed the NFT eigengene greater than mean + 3 s.d. The remaining 86% of cells had upregulated the NFT eigengene (4%, 34% and 48% mean + 1 s.d., 2 s.d. and 3 s.d., respectively), but did not reach >mean + 3 s.d. criteria. Overall, our data indicate significant overlap in cells coexpressing the senescence and NFT eigengenes; all neurons that expressed the NFT eigengene coexpressed the senescence eigengene greater than those without NFTs. Moreover, 99% of neurons that expressed the senescence eigengene coexpressed the NFT eigengene greater than those that were not senescent. Thus, senescent and NFT-bearing neurons overlap.

The association between senescence and stage of AD was also evaluated. Across eigengenes, the numbers of identified senescent cells per brain and AD stages were not significantly associated except for astrocytes, and only with the SRP eigengene. The number of astrocytes that expressed the SRP eigengene (that is, inflammation/SASP) was higher in the 24 individuals that Mathys et al.[19] reported to have early or late AD pathology compared with the 24 individuals without pathology (that is, 107 versus 61 cells, P value adjusted for testing multiple cell types <0.003). Astrocytes expressing SRP were also more abundant in the 24 individuals in Braak stage IV to VI compared with the 24 individuals Braak stage I to III (that is, 60 versus 108 cells, adjusted P value <0.02). Since the number of astrocytes expressing the CSP or SIP were similar between groups, we interpret that these cells were not fully senescent. Instead, they may have been in transition to becoming senescent or displayed a proinflammatory stress response not linked to senescence.

To gain insight into the mechanistic regulators of the senescence phenotype, we determined the weight that each gene contributed to their respective senescence eigengenes (CSP: Fig. 4a; SIP and SRP: Supplementary Fig. 6 and Supplementary Table 1). *CDKN2D* contributed most to the CSP eigengene (Fig. 4a). The average value of normalized *CDKN2D* expression in the three cell clusters that were

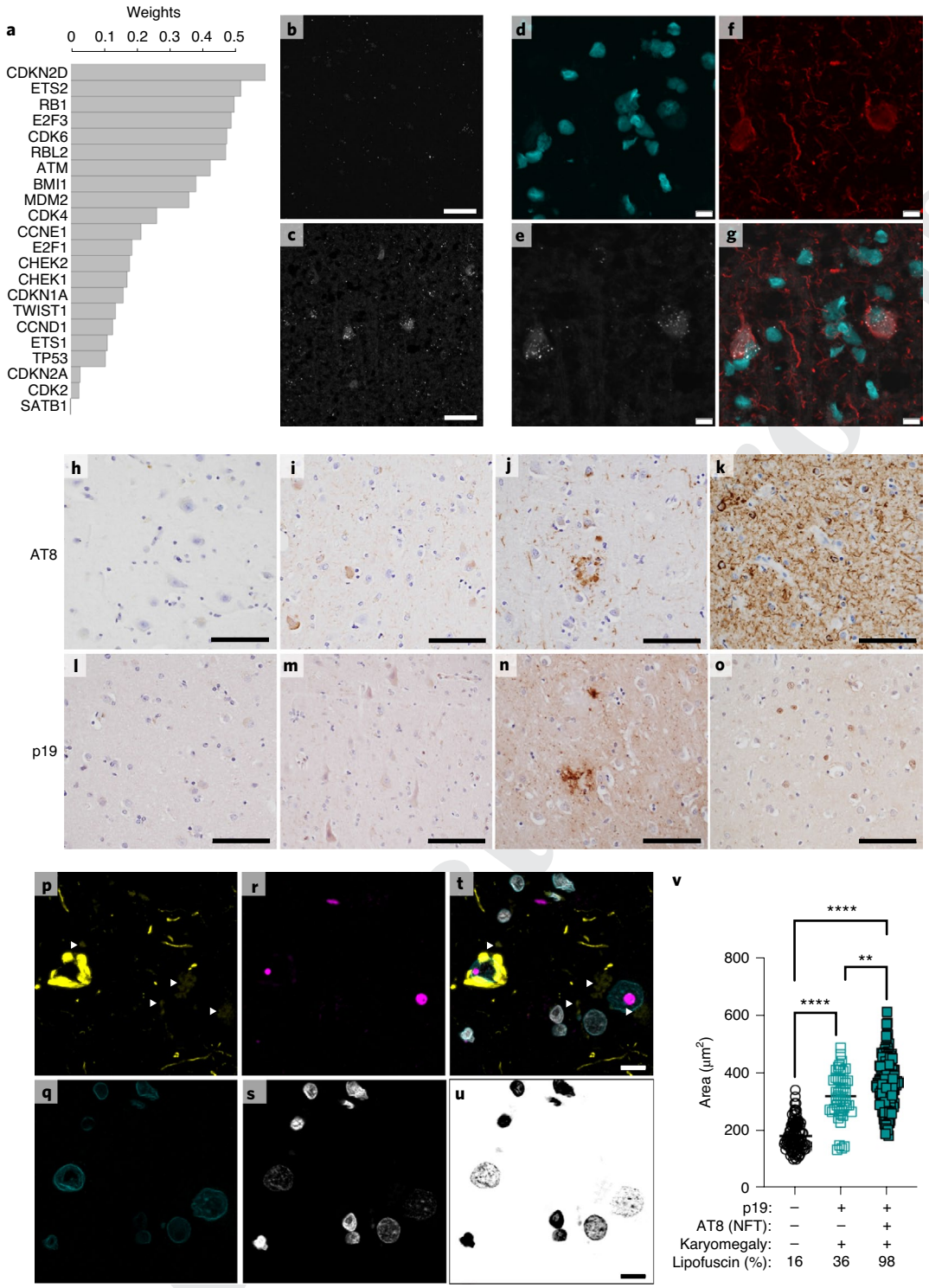

Fig. 4 | Upregulated *CDKN2D* and p19 deposition co-occur with tau neuropathology and morphological characteristics of cellular senescence in human AD. a, Weight of each gene in the CSP eigengene based on principal component analysis; *CDKN2D* had the highest weight. **b**,**c**, RNAscope probe *CDKN2D* in control (**b**) and AD (**c**) brains was performed on $n=3$ control and $n=3$ AD cases. Scale bar, 50 µm. **d**–**g**, RNAscope colabeled nuclei (**d**), *CDKN2D* (**e**), AT8 (phosphorylated tau, NFTs) (**f**) and color merged images (**g**). Scale bars, 10 µm. **h**–**o**, Representative images of frontal cortex in control (**h**, $n=2$) and AD neuropathologic change ($n=9$) cases (**i**–**k**) stained with (**h**–**k**) AT8 and adjacent section stained with anti-p19 antibody (**l**–**o**) (corresponding AT8 stains are directly above p19 stains). Scale bar, 80 µm. **p**–**t**, Coimmunofluorescence staining with AT8 (**p**), nuclear membrane lamin B1 (**q**), p19 (**r**) and Hoechst nuclear stain (**s**); overlap of all channels (**t**). **u**, Color-inverted Hoechst nuclear image for purposes of better visualizing nuclear morphology. Open black arrow, nuclei without p19 or NFTs; open cyan arrow, nuclei with p19; closed arrowhead, nuclei with p19 with NFTs. Scale bar, 10 µm. **v**, Quantification of cell nucleus area across cells without p19 or NFT staining (control) or expressing p19 with or without NFTs (as indicated in **u**). Characteristic lipofuscin autofluorescence (white arrowheads in **p** and **t**) was also quantified. Data presented as mean ± s.e.m. One way analysis of variance with Tukey's multiple comparisons test. ** $P=0.0031$, **** $P<0.0001$. *n* (number of cells), Control (p19-negative, AT8 negative): 101, p19 only: 44, p19+NFTs: 164.

enriched in senescent neurons (Supplementary Fig. 7) was 0.1, which was 1.4-fold higher than the excitatory neurons in other clusters (–$\log_{10}$ P value from the Wilcoxon rank sum test >15). Profiling single cells based on only elevated *CDKN2D* expression resulted in a similar cellular composition as with the senescence eigengenes (that is, predominantly excitatory neurons; Extended Data Fig. 6). However, the number of senescent excitatory neurons was overestimated in this analysis (*CDKN2D*: 2,731 versus CSP eigengene: 1,485) to indicate that not all cells with elevated *CDKN2D* could be considered senescent.

RNAscope indicated elevated *CDKN2D* expression in AD cases compared with controls (Fig. 4b,c and Extended Data Fig. 7), localization in neurons (Extended Data Fig. 8) and overlap with NFTs (Fig. 4d–g and Supplementary Fig. 12). Immunohistochemistry confirmed expression of the *CDKN2D* protein product, p19, in postmortem human AD with NFTs (Fig. 4h–o). The proportion of p19-positive cells ranged from 4% to 22% (Supplementary Table 4), consistent with estimates of the eigengene (Fig. 1). Staining revealed p19 expression in the nucleus, neuropil and in neuritic plaques of some AD cases (Fig. 4l–o). Coimmunofluorescence with Map2 (that is, neurons; Supplementary Fig. 9) or AT8 (that is, NFTs; Fig. 4t) with p19 indicated 30% of total neurons and 72% of those with NFTs neurons coexpressed p19. Karyomegaly[3,37] and lipofuscin[38] represent characteristic senescence morphologies and lysosomal degradation byproducts, respectively. They are not linked to specific marker genes, and thus allow for an unbiased validation of senescence. These analyses indicated that p19-expressing neurons had nuclei that were 1.8-fold larger than those of p19-negative neurons, and nuclei size was increased further by the presence of NFTs ($P<0.0001$ and $P=0.0031$, respectively; Fig. 4v). Similarly, twice as many p19-expressing neurons contained lipofuscin deposits than p19-negative neurons; this proportion increased to 98% in the presence of NFTs (Fig. 4v and Supplementary Fig. 13). Costaining with anti-lamin b1 to visualize the nuclear membrane further highlighted aberrant nuclear morphology in p19-positive cells (Fig. 4q,s–u and Supplementary Fig. 14), consistent with previous reports in AD[39], senescence[40] and our eigengene prediction (Supplementary Fig. 6b).

In summary, we developed, tested and validated the eigengene approach to identify senescent cells in transcriptomic datasets. Data from five separate human brain cohorts, six senescence transcriptomic profiles, two neuropathology profiles and RNA and protein histological methods indicated that excitatory neurons with upregulated *CDKN2D*/p19 and NFT neuropathology represent a unique cell population in human AD brains with morphological features consistent with senescence. Future studies are needed to validate and identify additional biomarkers, and to explain the interaction between p19 and tau pathology in senescence. While our data provide early insight into the heterogeneity of senescence marker genes and cell types in the brain, they also caution against reliance on SASP alone for identifying senescence in the brain. Specifically, astrocytes and endothelial cells upregulated SASP genes in the absence of other senescence hallmarks. Overall, the findings emphasize the utility and importance of applying multianalyte approaches when studying complex, dynamic cellular stress responses. Using these validated eigengenes in future studies may help guide senescence profiling across human tissues.

Methods

Ethics Oversight. Our research complies with all relevant ethical regulations. Postmortem tissues used for immunohistochemistry and immunofluorescence were provided by the Biggs Institute Brain Bank, which collected donor tissue in accordance with the University of Texas Health San Antonio Institutional Review Board. Postmortem tissue used for RNAScope was obtained from the Massachusetts Alzheimer's Disease Research Center (ADRC), which collected donor tissue in accordance with the Massachusetts General Hospital (MGH) Institutional Review Board.

snRNA-Seq and scRNA-Seq datasets. In this study, we refer to two snRNA-Seq datasets generated by Mathys et al.[19] and Zhou et al.[20] as cohort 1 and cohort 2, respectively. Datasets were accessed through Accelerating Medicines Partnership–AD (AMP–AD[41]) with Synapse IDs syn18485175 and syn21126462, respectively. The data included around 80,000 (ref. [19]) and around 70,000 (ref. [20]) single nuclei derived from the dorsolateral prefrontal cortex of 48 and 32 postmortem human brain samples, respectively. These data were provided by the longitudinal cohort studies of aging and dementia: the Religious Order Study (ROS) and the Rush Memory and Aging Project (MAP)[42]. Inclusion criteria were the same as in the data-generating studies. Specifically, in cohort 1, 24 control individuals were selected with no or very little pathology in addition to 24 age-matched individuals with a spectrum of mild-to-severe β-amyloid and other pathologies[19]. The mean and median of age were 86 and 87 years old, respectively, with s.d. of 5 years. In cohort 2, 11 people with AD carrying TREM2-CV, 10 people with AD carrying TREM2-R62H and 11 age-matched controls were included[20]. The mean and median of age were 89 years old with s.d. of 6 years. Four subjects (10248033, 20207013, 10290265 and 11072071) were represented in both datasets. We included them only in cohort 1 but not in cohort 2; in total around 140,000 cells from 76 brains were analyzed (Supplementary Table 2). Embryonic brains are not expected to have a significant senescence burden and, thus, can be appropriate controls for our study. We used the scRNA-Seq data of around 4,000 cells that Fan et al.[21] generated from cerebral cortex of two female twin embryos of age 22 and 23 weeks. Neurons are often excluded from scRNA-Seq datasets due to their large size; similarly senescent cells undergo excess growth[3,37] and may also be excluded from scRNA-Seq profiling. Nevertheless, to assess the extensibility of our approach, we analyzed the scRNA-Seq data of around 13,000 cells that Grubman and colleagues generated from the entorhinal cortex of 12 individuals[27] (Supplementary Figs. 2, 10 and 11).

Eigengene analysis. We downloaded snRNA-Seq data from the studies of Mathys et al.[19] and Zhou et al.[20], which were available from the AMP–AD[41] website, using the synapser (https://r-docs.synapse.org/articles/synapser.html) R package[43] (v.0.6.61) and custom R scripts[44] (v.3.6.1). We downloaded clinical data from the corresponding publication pages. For each of the three gene sets in the Supplementary Table 1 (refs. [3,34]) we used the compute.pigengene() function from the Pigengene package (v.1.13.4) to compute an eigengene[18], which is a weighted average expression over all genes in the corresponding list[17]. Following our previous approach on computing eigengenes[18,45–47], we balanced the number of cells in each cell type using oversampling, so that all cell types had comparable representatives in the analysis. Specifically, we repeated the data of each astrocyte 104, endothelial cell 2,919, excitatory neuron 10, inhibitory neuron 38, microglia 184, oligodendrocyte 19, oligodendrocyte precursor cell 134 and pericytes 2,115 times, and obtained 352,768; 353,199; 349,760; 349,448; 353,280; 346,465; 352,018 and 353,205 samples from each cell type, respectively. Weights were optimized using a principal component analysis. We computed the mean expression of each eigengene over all analyzed cells. Cells were considered senescent if their level of eigengene expression was more than the mean expression over all cells plus three times the s.d. Hypergeometric tests were used to identify the cell types in which senescent cells were overrepresented. We used the project.eigen() function from the Pigengene package to infer the eigengenes values in the validation datasets based on the same weights that we had obtained from our analysis on cohort 1 as the training dataset. To see how much senescence and NFT expressing eigengenes overlap, we visualized their expression in density plots using the ggplot2 package. A kernel density estimate was used to represent the probability density function of eigengene values (Fig. 3). We tested the significance of overlap between NFT cells and senescent cells with hypergeometric tests using the phyper function in R. We set the log.p parameter to TRUE to increase the reporting accuracy. Throughout this paper, we replaced the $\log_{10}$ of any P value between 0.1 and 1 with –0. Q13

Cell clustering. We applied the Seurat pipeline[48] to cluster the cells in cohort 1 based on their gene expression profile in an unbiased way, agnostic to senescence markers. First, we performed quality control and removed cells with less than 200, or more than 6,000, detected genes. We also removed genes expressed in fewer than three cells. Then, we normalized the raw counts using the sctransform method in Seurat, which applied a regularized negative binomial regression modeling approach for the normalization and variance stabilization of molecular counts[49]. We used the RunPCA() function to identify the top 3,000 most variable genes, the FindNeighbors() function to construct a K-nearest neighbor graph based on the Euclidean distance calculated from the top 30 principal components[50], and the FindClusters() function to identify cell clusters based on the Louvain algorithm[51]. We set the resolution parameter for the clustering granularity as 0.8. To visualize the cell clusters, we used the uniform manifold approximation and projection method for nonlinear dimensional reduction[52]. For each cell cluster, we performed Fisher's exact test to assess its enrichment in the cells that we had previously identified as senescent based on our eigengene approach.

Immunohistochemical staining. Immunohistochemical (IHC) stains were performed using a Thermo Scientific Lab Vision Autostainer 480 following deparaffinization of formalin-fixed paraffin-embedded sections (FFPE) and 30 min of heat-induced antigen retrieval in citrate buffer. Endogenous peroxidase was blocked by immersion in 3% hydrogen peroxide for 10 min, then rinsing. A protein

block for 15 min with 2.5% normal goat serum (Sigma) was then performed. After rinsing, sections were incubated with either mouse anti-human monoclonal AT8 antibody (Thermo Scientific) at 1:2,000 or rabbit polyclonal anti-p19 antibody (Abcam) at 1:100 for 45 min, washed and incubated with undiluted secondary antibody (goat anti-mouse or goat anti-rabbit, respectively, IgG (HRP), VisUCyte) for 45 min followed by rinsing. Diaminobenzidine (DAB) chromagen (BD Pharmigen) was used to visualize immunoreactivity. IHC staining for p19 was performed on FFPE sections of the middle frontal gyrus from six AD cases, all of which demonstrated a high level of AD neuropathologic change with a Braak stage of VI, three intermediate ADNC level cases and two primary age-related tauopathy (PART) control cases (Braak stages I–II) with no neocortical neurofibrillary tangles.

Immunofluorescence for colabeling. For dual labeling immunofluorescence, human brain sections were deparaffinized via xylene and hydrated in a series of graded alcohol. We performed heat-induced antigen retrieval using a pressure cooker and 10 mM sodium citrate (pH 6.6) with 0.2% Tween. Sections were then exposed to light-emitting diode light overnight in 10 mM sodium citrate (pH 6.6) with 0.2% Tween and 0.05% sodium azide in 4 °C and blocked using 0.25% bovine serum albumin (BSA) and PBS + 0.2% Triton-X100 (PBSTr) for 2 h at room temperature. Primary antibodies were added at the following concentrations, p19 (1:100, ab26287, Abcam) and MAP2 (1:200, PA5-17646, Invitrogen) and incubated overnight at 4 °C. Sections were washed three times in PBSTr each for 10 min at room temperature. Alexa Fluor-conjugated secondary antibodies (ThermoFisher Scientific) diluted in 0.25% BSA and PBSTr (1:200) were then added and the sections incubated for 2 h at room temperature. Sections were washed three times with PBSTr and incubated with 0.3% Sudan Black in 70% ethanol for 10 min and washed ten times with PBS at room temperature. Slides were mounted using 4,6-diamidino-2-phenylindole (DAPI) Fluromount-G (0100-20, Southern Biotech). For AT8 and p19 costaining, we used Phospho-Tau (Ser202,Thr205) (ThermoFisher Scientific, MN1020, conjugated with AF594 using Alexa Fluor 594 Antibody Labeling Kit catalog no. A20185) and P19 INK4d (ab262871, indirect labeling with Alexa Fluor 647 Tyramide Reagent, catalog no. B40958). Syto83 was used as a nuclear counterstain as described previously[53]. Images were acquired using an Olympus FluoView FV1200 confocal laser scanning microscope. For quad labeling p19, lamin B1 AT8 and Hoechst straining, following the p19 Tyramide boost step (anti-CDKN2D Sigma catalog no. HPA043546; same clone as ab262871), slides were microwave-treated in citrate buffer until boiling (100% power for 127 s) followed by 20% power for 15 min, then cooled for 25 min at room temperature. Slides were placed in a humidity chamber, blocked with 10% normal goat serum for 1 h, then incubated in primary antibodies: mouse monoclonal lamin b1, clone 10H34L18, 1:500 (ThermoFisher Scientific, catalog no. 702972) and AT8 1:1000 (ThermoFisher Scientific, catalog no. MN1020) in CST antibody diluent overnight (18 h) at 4 °C. The following day, slides were washed in TBS-T and incubated with secondary antibodies (IgG (H + L) highly cross-absorbed goat anti-rabbit, Alexa Fluor Plus 647 (catalog no. A32733) and IgG (H + L) highly cross-absorbed goat anti-mouse, Alexa Fluor Plus 555 (catalog no. A32727)) diluted 1:1500 in TBS-T for 2 h at room temperature. Slides were rinsed twice in TBS-T and incubated in Hoechst 33342 (ThermoFisher Scientific, EdU Imaging Kit Component G, catalog no. C10337) 1:2,000 in TBS-T for 30 min at room temperature. Slides were rinsed twice in TBS-T and coverslipped using ProLong Gold Antifade Reagent (ThermoFisher Scientific, catalog no. P36934), sealed with nail polish and imaged with an Olympus FluoView FV1200 confocal laser scanning microscope.

RNAscope. Fresh frozen temporal cortex (Brodmann area 20) was obtained from the Massachusetts ADRC, which collected donor tissue in accordance with the MGH Institutional Review Board. AD subjects ($n = 3$) met clinical and neuropathologic criteria for AD and control subjects ($n = 3$) did not have clinical or neuropathologic evidence of neurodegenerative disease (Supplementary Table 5). Cryostat sections were sliced at 8 µm and placed on SuperFrost plus slides. Sections were fixed for 15 min in chilled 4% paraformaldehyde in PBS and then rinsed in PBS and dehydrated in an ascending ethanol series (50%, 70% and 100% twice for 5 min each). RNAscope was then performed using the RNAScope Multiplex Fluorescent V2 Assay (ACD Bio) and HybEZ II Hybridization System (ACD Bio) according to the manufacturer's recommendations with the following modification: treatment with protease IV (ACD Bio) was carried out for 5 min at room temperature. A custom 18 ZZ probe was designed to target a 315–1378 bp region of CDKN2d (GenBank accession: NM_001800.4; catalog no. 1098101-c1; ACD Bio). Following in situ hybridization, sections were blocked in 5% BSA (Sigma Aldrich) for 1 h and then mouse anti-HuD (E-1; catalog no. sc-28299; Santa Cruz Biotechnology) was applied overnight. The following day, donkey anti-mouse Alexa750 (catalog no. ab175738; Abcam) was applied and then mouse anti-tau-biotin conjugated (AT8; catalog no. MN1020b; ThermoFisher Scientific) was applied and incubated overnight. AT8 was detected with streptavidin-Alexa555. All antibodies were applied at a 1:500 concentration. Sections were then coverslipped with Fluoromount G with DAPI (Southern Biotech) and sealed with nail polish. Images were acquired using an Olympus Confocal FV3000 and an Olympus VS120 slide scanner.

Image quantification. IHC color images were scored manually by a technician blinded to cases. Total cells and p19-positive cells were counted on a minimum of two representative images. The images were preselected by a neuropathologist to ensure similar brain regions were represented across cases. To determine colocalization of p19, confocal images were analyzed by a technician blinded to cases. Cell nuclei and lipofuscin measures were quantified from coimmunofluorescent images using Adobe Photoshop v.22.3.0. Neurons were chosen at random and categorized by the presence or absence of p19 and AT8 staining. Each neuron's nuclei and lipofuscin area were measured using the Histogram tool. Cells for lamin B1 quantification were selected from confocal z-stack images opened in ImageJ. To ensure cells were profiled from a mid-cell plane (that is, not on edges) morphology parameters were applied (that is, size: 85 µm^2–infinity, with gray scale thresholding 475–65535 and default circularity: 0.00–1.00). The ROI Manager was used to acquire data from individual cells. The corrected total cell fluorescence (CTCF) was calculated (CTCF = integrated density – area of selected cell), plotted and analyzed with the aid of GraphPad Prism Software v.9.1.0.

Statistics and reproducibility. No statistical method was used to predetermine sample size. No data were excluded from the analyses. Exact n values are reported in respective figure legends. Reproducibility measures included analyses of initial and validation datasets (that is, senescence: Cohort 1, Cohort 2, embryo control and NFTs: Dunckley and Garcia); hypothesis testing by applying multiple, distinct bioinformatic approaches on each dataset; evaluating distinct datasets generated by independent laboratories; comparing results between distinct transcriptomic technologies (snRNA-Seq and scRNA-Seq); confirming senescence eigengene results from multiple gene lists generated by our group (CSP, SIP and SRP) and those derived from publicly available senescence gene lists (KEGG, GO and CellAge); reproducing histology experiments using multiple biological replicates (postmortem human brains $n = 5$ control and $n = 12$ AD) derived from separate brain biorepositories (Biggs Institute Brain Bank and Massachusetts ADRC), across four laboratories (for example, Walker, Frost, Bennett and Orr) located in three separate institutions (UTHSA, MGH and Wake Forest School of Medicine); applying multiple, complementary, histological techniques to confirm bioinformatic findings (RNAscope, immunohistochemistry and immunofluorescence). The investigators that analyzed/quantified the tissues were blinded to disease diagnosis (AD or control).

Reporting Summary. Further information on research design is available in the Nature Research Reporting Summary linked to this article.

Data availability

The snRNA-Seq data analyzed in this study are available from https://www.synapse.org/ with synapse IDs: syn18485175 and syn21126462 for cohorts 1 and 2, respectively. Accessing these data requires submitting a Data Use Certificate through the AMP–AD website. Clinical data were available in the corresponding publications. The scRNA-Seq data from the embryonic cortex and the scRNA-Seq data from the entorhinal cortex are also available from the Gene Expression Omnibus[54] with accession numbers GSE103723 and GSE138852. Q15

Code availability

Our R scripts, which are available as Supplementary material, can be used to fully reproduce our results. Our code is also publicly available at https://bitbucket.org/habilzare/alzheimer/src/master/code/senescence/Shiva/.

Received: 5 November 2020; Accepted: 26 October 2021;

References

1. Tchkonia, T., Zhu, Y., van Deursen, J., Campisi, J. & Kirkland, J. L. Cellular senescence and the senescent secretory phenotype: therapeutic opportunities. *J. Clin. Invest.* **123**, 966–972 (2013).
2. Acosta, J. C. et al. A complex secretory program orchestrated by the inflammasome controls paracrine senescence. *Nat. Cell Biol.* **15**, 978–990 (2013).
3. Musi, N. et al. Tau protein aggregation is associated with cellular senescence in the brain. *Aging Cell* **17**, e12840 (2018).
4. Chow, H. M. et al. Age-related hyperinsulinemia leads to insulin resistance in neurons and cell-cycle-induced senescence. *Nat. Neurosci.* **22**, 1806–1819 (2019).
5. Ogrodnik, M. et al. Obesity-induced cellular senescence drives anxiety and impairs neurogenesis. *Cell Metab.* **29**, 1061–1077 e1068 (2019).
6. Riessland, M. et al. Loss of SATB1 induces p21-dependent cellular senescence in post-mitotic dopaminergic neurons. *Cell Stem Cell* **25**, 514–530 e518 (2019).
7. Chinta, S. J. et al. Cellular senescence is induced by the environmental neurotoxin paraquat and contributes to neuropathology linked to Parkinson's disease. *Cell Rep.* **22**, 930–940 (2018).

8. Bussian, T. J. et al. Clearance of senescent glial cells prevents tau-dependent pathology and cognitive decline. *Nature* **562**, 578–582 (2018).
9. Zhang, P. et al. Senolytic therapy alleviates Aβ-associated oligodendrocyte progenitor cell senescence and cognitive deficits in an Alzheimer's disease model. *Nat. Neurosci.* **22**, 719–728 (2019).
10. Justice, J. N. et al. Cellular senescence biomarker p16INK4a+ cell burden in thigh adipose is associated with poor physical function in older women. *J. Gerontol. A Biol. Sci. Med. Sci.* **73**, 939–945 (2018).
11. Hickson, L. J. et al. Senolytics decrease senescent cells in humans: preliminary report from a clinical trial of Dasatinib plus Quercetin in individuals with diabetic kidney disease. *EBioMedicine* **47**, 446–456 (2019).
12. Gillispie, G. J. Evidence of the cellular senescence stress response in mitotically active brain cells – implications for cancer and neurodegeneration.*Life (Basel)* **11**, 153 (2021).
13. Sah, E. The cellular senescence stress response in post-mitotic brain cells – cell survival at the expense of tissue degeneration. *Life (Basel)* **11**, 229 (2021).
14. Arendt, T., Rodel, L., Gartner, U. & Holzer, M. Expression of the cyclin-dependent kinase inhibitor p16 in Alzheimer's disease. *Neuroreport* **7**, 3047–3049 (1996).
15. Katsouri, L. et al. Ablation of reactive astrocytes exacerbates disease pathology in a model of Alzheimer's disease. *Glia* **68**, 1017–1030 (2020).
16. Hansen, D. V., Hanson, J. E. & Sheng, M. Microglia in Alzheimer's disease. *J. Cell Biol.* **217**, 459–472 (2018).
17. Oldham, M. C., Horvath, S. & Geschwind, D. H. Conservation and evolution of gene coexpression networks in human and chimpanzee brains. *Proc. Natl Acad. Sci. USA* **103**, 17973–17978 (2006).
18. Foroushani, A. et al. Large-scale gene network analysis reveals the significance of extracellular matrix pathway and homeobox genes in acute myeloid leukemia: an introduction to the Pigengene package and its applications. *BMC Med. Genomics* **10**, 16 (2017).
19. Mathys, H. et al. Single-cell transcriptomic analysis of Alzheimer's disease. *Nature* **570**, 332–337 (2019).
20. Zhou, Y. et al. Human and mouse single-nucleus transcriptomics reveal TREM2-dependent and TREM2-independent cellular responses in Alzheimer's disease. *Nat. Med.* **26**, 131–142 (2020).
21. Fan, X. et al. Spatial transcriptomic survey of human embryonic cerebral cortex by single-cell RNA-seq analysis. *Cell Res.* **28**, 730–745 (2018).
22. Bryant, A. G. et al. Cerebrovascular senescence is associated with tau pathology in Alzheimer's disease. *Front. Neurol.* **11**, 575953 (2020).
23. Bhat, R. et al. Astrocyte senescence as a component of Alzheimer's disease. *PLoS ONE* **7**, e45069 (2012).
24. Tchkonia, T. & Kirkland, J. L. Aging, cell senescence, and chronic disease: emerging therapeutic strategies. *JAMA* **320**, 1319–1320 (2018).
25. Hooper, A. T. et al. Angiomodulin is a specific marker of vasculature and regulates vascular endothelial growth factor-A-dependent neoangiogenesis. *Circ. Res.* **105**, 201–208 (2009).
26. Boraas, L. C. & Ahsan, T. Lack of vimentin impairs endothelial differentiation of embryonic stem cells. *Sci. Rep.* **6**, 30814 (2016).
27. Grubman, A. et al. A single-cell atlas of entorhinal cortex from individuals with Alzheimer's disease reveals cell-type-specific gene expression regulation. *Nat. Neurosci.* **22**, 2087–2097 (2019).
28. Avelar, R. A. et al. A multidimensional systems biology analysis of cellular senescence in aging and disease. *Genome Biol.* **21**, 91 (2020).
29. Ashburner, M. et al. Gene ontology: tool for the unification of biology. The Gene Ontology Consortium. *Nat. Genet.* **25**, 25–29 (2000).
30. Gene Ontology, C. The Gene Ontology resource: enriching a GOld mine. *Nucleic Acids Res.* **49**, D325–D334 (2021).
31. Kanehisa, M. & Goto, S. KEGG: Kyoto encyclopedia of genes and genomes. *Nucleic Acids Res.* **28**, 27–30 (2000).
32. Orr, M. E., Sullivan, A. C. & Frost, B. A brief overview of tauopathy: causes, consequences, and therapeutic strategies. *Trends Pharmacol. Sci.* **38**, 637–648 (2017).
33. Fu, H. et al. A tau homeostasis signature is linked with the cellular and regional vulnerability of excitatory neurons to tau pathology. *Nat. Neurosci.* **22**, 47–56 (2019).
34. Dunckley, T. et al. Gene expression correlates of neurofibrillary tangles in Alzheimer's disease. *Neurobiol. Aging* **27**, 1359–1371 (2006).
35. Otero-Garcia, T. *et al.* Single-soma transcriptomics of tangle-bearing neurons in Alzheimer's disease reveals the signatures of tau-associated synaptic dysfunction. Preprint at *bioRxiv* https://doi.org/10.1101/2020.05.11.088591 (2020).
36. Furcila, D., Dominguez-Alvaro, M., DeFelipe, J. & Alonso-Nanclares, L. Subregional density of neurons, neurofibrillary tangles and amyloid plaques in the hippocampus of patients with Alzheimer's disease. *Front. Neuroanat.* **13**, 99 (2019).
37. Neurohr, G. E. et al. Excessive cell growth causes cytoplasm dilution and contributes to senescence. *Cell* **176**, 1083–1097.e1018 (2019).
38. Georgakopoulou, E. A. et al. Specific lipofuscin staining as a novel biomarker to detect replicative and stress-induced senescence. A method applicable in cryo-preserved and archival tissues. *Aging (Albany NY)* **5**, 37–50 (2013).
39. Frost, B., Bardai, F. H. & Feany, M. B. Lamin dysfunction mediates neurodegeneration in tauopathies. *Curr. Biol.* **26**, 129–136 (2016).
40. Barascu, A. et al. Oxidative stress induces an ATM-independent senescence pathway through p38 MAPK-mediated lamin B1 accumulation. *EMBO J.* **31**, 1080–1094 (2012).
41. Hodes, R. J. & Buckholtz, N. Accelerating medicines partnership: Alzheimer's disease (AMP–AD) knowledge portal aids Alzheimer's drug discovery through open data sharing. *Expert Opin. Ther. Targets* **20**, 389–391 (2016).
42. Bennett, D. A. et al. Religious orders study and rush memory and aging project. *J. Alzheimers Dis.* **64**, S161–S189 (2018).
43. R Core Team. R.: *A language and environment for statistical computing* https://www.R-project.org/ (2013).
44. R Core Team. R: a language and environment for statistical computing. (R Foundation for Statistical Computing, 2017).
45. Zainulabadeen, A., Yao, P. & Zare, H. Underexpression of specific interferon genes is associated with poor prognosis of melanoma. *PLoS ONE* **12**, e0170025 (2017).
46. Agrahari, R. et al. Applications of Bayesian network models in predicting types of hematological malignancies. *Sci. Rep.* **8**, 6951 (2018).
47. Samimi, H. DNA methylation analysis improves the prognostication of acute myeloid leukemia. *eJHaem* **2**, 211–218 (2021).
48. Butler, A., Hoffman, P., Smibert, P., Papalexi, E. & Satija, R. Integrating single-cell transcriptomic data across different conditions, technologies, and species. *Nat. Biotechnol.* **36**, 411–420 (2018).
49. Hafemeister, C. & Satija, R. Normalization and variance stabilization of single-cell RNA-seq data using regularized negative binomial regression. *Genome Biol.* **20**, 296 (2019).
50. Altman, N. S. An introduction to kernel and nearest-neighbor nonparametric regression. *Am. Stat.* **46**, 175–185 (1992).
51. Blondel, V. D., Guillaume, J.-L., Lambiotte, R. & Lefebvre, E. Fast unfolding of communities in large networks. *J. Stat. Mech.* **2008**, P10008 (2008).
52. McInnes, L., Healy, J. & Melville, J. Umap: Uniform manifold approximation and projection for dimension reduction. Preprint at *arXiv* (2018).
53. Merritt, C. R. et al. Multiplex digital spatial profiling of proteins and RNA in fixed tissue. *Nat. Biotechnol.* **38**, 586–599 (2020).
54. Edgar, R., Domrachev, M. & Lash, A. E. Gene Expression Omnibus: NCBI gene expression and hybridization array data repository. *Nucleic Acids Res.* **30**, 207–210 (2002).

Acknowledgements

This work is supported by NIH/NIA (R01AG068293, R01AG057896, U01AG046170, RF1AG057440, R01AG057907, K99AG061259; P30AG062421; RF1AG051485, R21AG059176, and RF1AG059082 and T32AG021890), Cure Alzheimer's Fund and Veterans Affairs (K2BX003804). We obtained ROSMAP data from the AD Knowledge Portal (https://adknowledgeportal.synapse.org). Study data were provided by the Rush Alzheimer's Disease Center, Rush University Medical Center, Chicago. Data generation was supported by National Institute on Aging (NIA) and grants RF1AG57473, P30AG10161, R01AG15819, R01AG17917, U01G46152, U01AG61356 and RF1AG059082. Additional phenotypic ROSMAP data can be requested at https://www.radc.rush.edu. We acknowledge the Texas Advanced Computing Center (TACC) at the University of Texas at Austin for providing high-performance computing resources: http://www.tacc.utexas.edu. We acknowledge the Biggs Institute Brain Bank and Massachusetts ADRC for providing postmortem human tissue for analyses. The funders had no role in study design, data collection and analysis, decision to publish or preparation of the manuscript.

Author contributions

All authors edited and approved the final manuscript. In addition, S.K.D. developed code, designed and performed in silico experiments, performed all bioinformatic and statistical analyses, prepared figures and drafted the manuscript; J.W. provided tissue from the Biggs Brain Bank, performed p19 and AT8 IHC validation and wrote IHC methods; E.S. performed immunofluorescence validation (p19, AT8 and lamin B1), performed confocal microscopy and wrote the corresponding methods; E.B. performed blinded analyses of IHC and immunofluorescence and wrote the corresponding methods; F.A. performed immunofluorescence (p19, AT8 and Map2) validation and wrote corresponding methods; B.F. provided oversight to F.A. and provided Lamin b1 expertise; B.W. performed RNAScope; R.E.B. requested and acquired brain tissue from MGH ADRC, performed confocal microscopy, provided oversight to B.W., generated RNAscope figures and wrote RNAscope methods, RNAscope data interpretation; T.C.O. developed methods to analyze lamin b1 expression, performed blinded lamin b1 analyses and wrote lamin B1 analyses methods; Y.Z. provided access and expertise on cohort 2 snRNA-Seq data; P.S.A. provided access and expertise on cohort 2 snRNA-Seq data; M.C. provided access and expertise on cohort 2 snRNA-Seq data; P.H.S. provided bioinformatics consultation and validation; P.X. performed cell clustering analyses and wrote corresponding methods; M.W. performed cell clustering analyses and wrote the

corresponding methods; B.Z. provided oversight to P.X. and provided bioinformatic consultation; H.Z. provided oversight to S.K.D. (bioinformatic experimental design and development), acquired access to all datasets, designed and confirmed bioinformatic data analyses and interpreted results; M.E.O. conceived the project, acquired funding, provided supervision (E.S., E.B. and T.C.O.), analyzed and interpreted histology data, interpreted bioinformatic data, and drafted manuscript and submitted the manuscript.

Competing interests

Patent applicant: Wake Forest University Health Sciences. Name of inventor: Miranda Orr. Application number: 63/199,927 & 63/261,630. Status of application: Pending. The specific aspect of manuscript covered in patent application: data from this manuscript was used to file a patent, 'Biosignature and therapeutic approach for neuronal senescence'.

Additional information

Supplementary information The online version contains supplementary material available at https://doi.org/10.1038/s43587-021-00142-3.

Correspondence and requests for materials should be addressed to Habil Zare or Miranda E. Orr.

Peer review information *Nature Aging* thanks Markus Riessland and the other, anonymous, reviewer(s) for their contribution to the peer review of this work.

Reprints and permissions information is available at www.nature.com/reprints.

Publisher's note Springer Nature remains neutral with regard to jurisdictional claims in published maps and institutional affiliations.

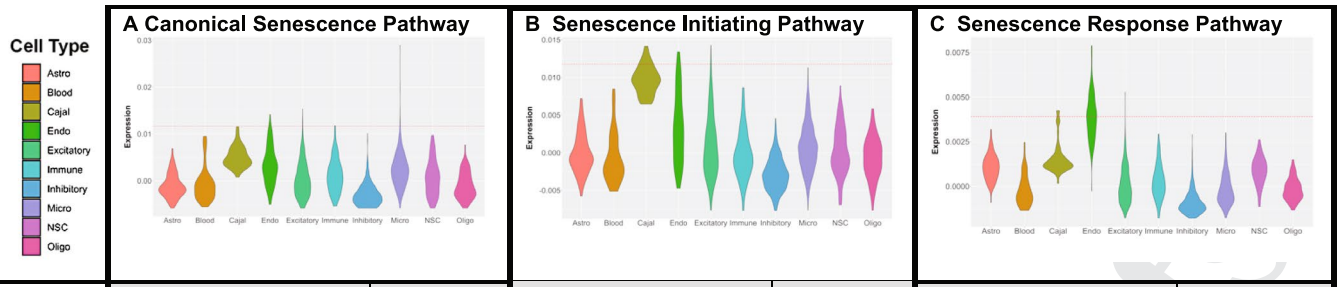

Cell Types	Cell Numbers		log10(p-value)	Cell Numbers		log10(p-value	Cell Numbers		log10(p-value
	Normal	Senescent		Normal	Senescent		Normal	Senescent	
Ast	111	0	0	111	0	0	111	0	0
Blood	60	0	0	60	0	0	60	0	0
Cajal	51	0	0	44	7	-80	49	2	-5.2
Endo	156	2	0.01	152	6	-36	81	77	-1087.5
Ext	1500	6	0.003	1496	10	-3	1503	3	0
Immune	94	1	0.01	95	0	0	95	0	0
Inh	948	0	0	948	0	0	948	0	0
Micro	719	7	0.009	726	0	0	726	0	0
NSC	102	0	0	102	0	0	102	0	0
Oligo	82	0	0	82	0	0	82	0	0
Total	3823	16		3816	23		3757	82	

Extended Data Fig. 1 | Prominent senescent cell types in prefrontal cortex of the embryonic control. Cell types and counts represented in the senescent cell population discovered in (A) CSP, (B) SIP and (C) SRP. The cutoff and statistical test definitions are the same as in Fig. 1. Cell populations: astrocytes [Ast], blood cells [Blood], Cajal-Retzius cells [Cajal], endothelial cells [Endo], excitatory neurons [Ext], immune cells [Immune], inhibitory neuron [Inh], microglia [Micro], neural stem cells [NSC], and oligodendrocyte precursor cells [Oligo] were classified in the original publication.

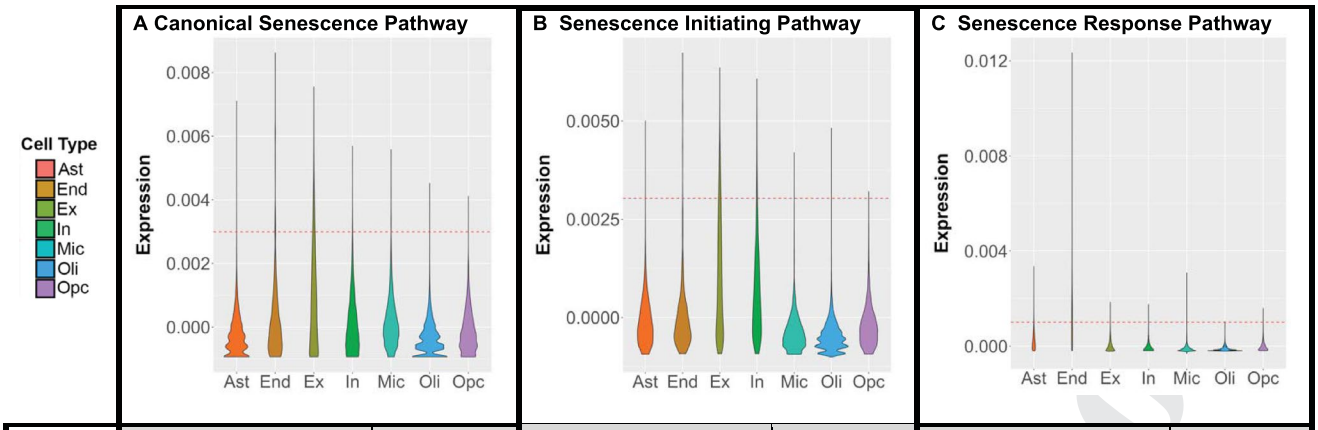

Cell Types	Cell Numbers		log10(p-value)	Cell Numbers		log10(p-value	Cell Numbers		log10(p-value
	Normal	Senescent		Normal	Senescent		Normal	Senescent	
Ast	8707	18	0	8708	17	0	8217	508	-1188.9
End	754	21	-5.1	766	9	-0.01	389	386	-3498.6
Ex	11363	1227	-4819.5	11288	1302	-4662.9	12558	32	0
In	3691	36	0	3580	147	-48.8	3718	9	0
Mic	3728	19	0	3742	5	0	3739	8	0
Oli	25366	5	0	25367	4	0	25370	1	0
Opc	2917	5	0	2921	1	0	2915	7	0
Total	56526	1331		56372	1485		56906	951	

Extended Data Fig. 2 | Prominent senescent cell types in the dorsal lateral prefrontal cortex in Cohort 2. Cell types and counts represented in the senescent cell population discovered in (A) CSP, (B) SIP and (C) SRP with n = 57,857. The cutoff, statistical test and abbreviations definitions are the same as in Fig. 1.

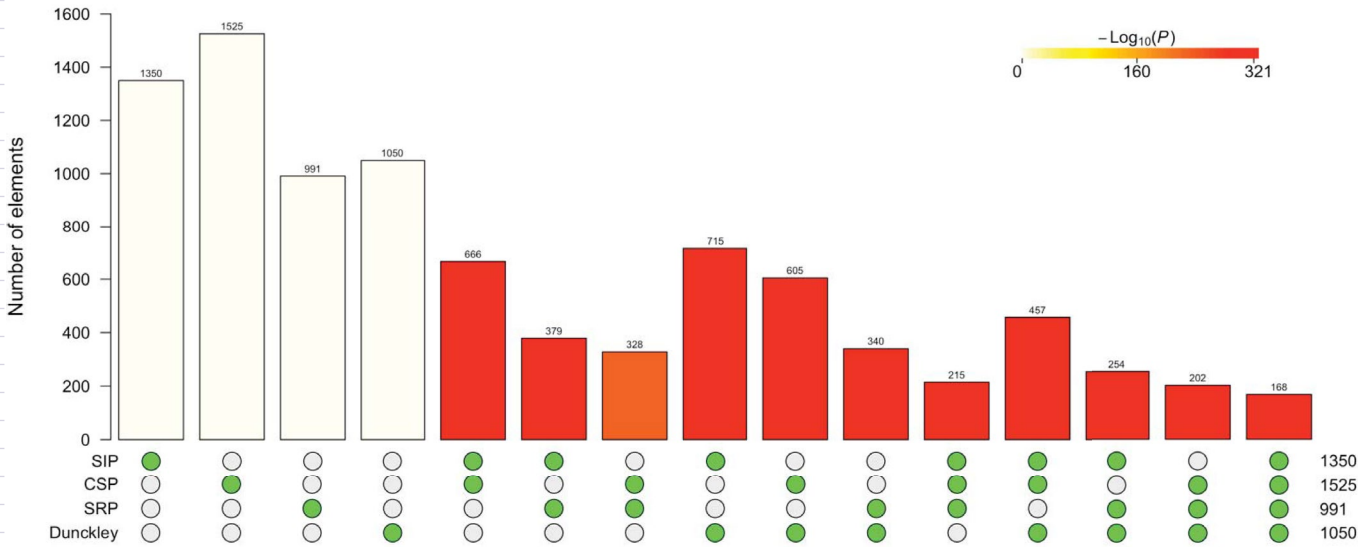

Extended Data Fig. 3 | Overlap between senescent and NFT neurons. Each vertical bar represents the number of neurons in Cohort 1 that express the eigengenes marked by green circles below the bar. Each row at the bottom corresponds to an eigengene, and the number of neurons expressing that eigengene is shown in the right end on each row. The probability distributions of multi-set intersections have been calculated and the significance was tested using a hypergeometric test. The scale bar at top right shows the level of significance for each intersection. The largest p-value is −232 in log10 scale, which corresponds to the intersection between SRP and CSP expressing cells.

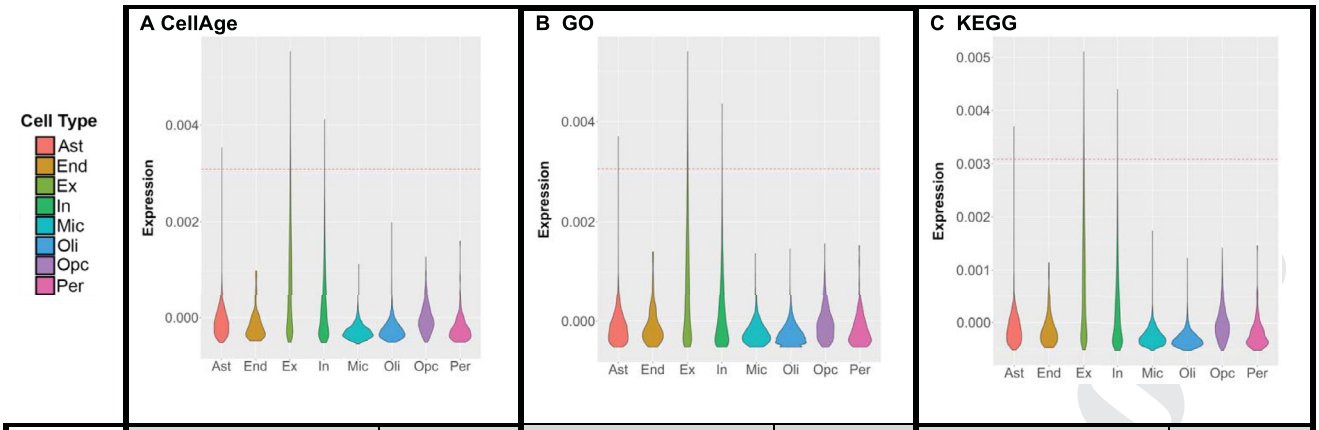

Cell Types	Cell Numbers		log10(p-value)	Cell Numbers		log10(p-value	Cell Numbers		log10(p-value
	Normal	Senescent		Normal	Senescent		Normal	Senescent	
Ast	3391	1	~0	3391	1	~0	3391	1	~0
End	121	0	0	121	0	0	121	0	0
Ex	33759	1217	-2534	33693	1283	-2673	33794	1182	-2277
In	9161	35	~0	9159	37	~0	9142	54	~0
Mic	1920	0	0	1920	0	0	1920	0	0
Oli	18235	0	0	18235	0	0	18235	0	0
Opc	2627	0	0	2627	0	0	2627	0	0
Per	167	0	0	167	0	0	167	0	0
Total	69381	1253		69313	1321		69397	1237	

Extended Data Fig. 4 | Prominent senescent cell types using CellAge, GO and KEGG gene lists in Cohort 1. Cell types and counts represented in the senescent cell population discovered in (A) CellAge, (B) GO and (C) KEGG. The cutoff, statistical test and abbreviations definitions are the same as in Fig. 1.

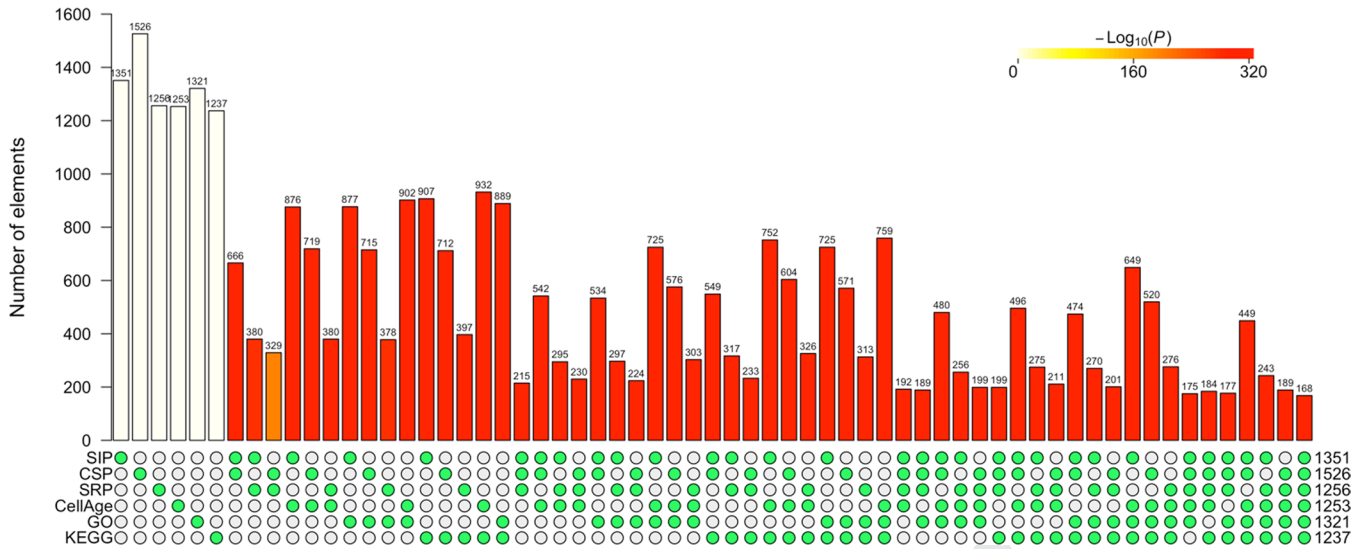

Extended Data Fig. 5 | Overlap between senescent cell populations. Each vertical bar represents the number of senescent cells in Cohort 1 that express the senescence eigengenes, marked by green circles below the bar. Each row at the bottom corresponds to a senescence eigengene, and the number of senescent cells expressing that eigengene is shown at the end of each row. The probability distributions of multi-set intersections have been calculated and the significance was tested using a hypergeometric test. The scale bar at top right shows the level of significance for each intersection. The largest p-value is-260 in log10 scale corresponding to the intersection of SRP and CSP.

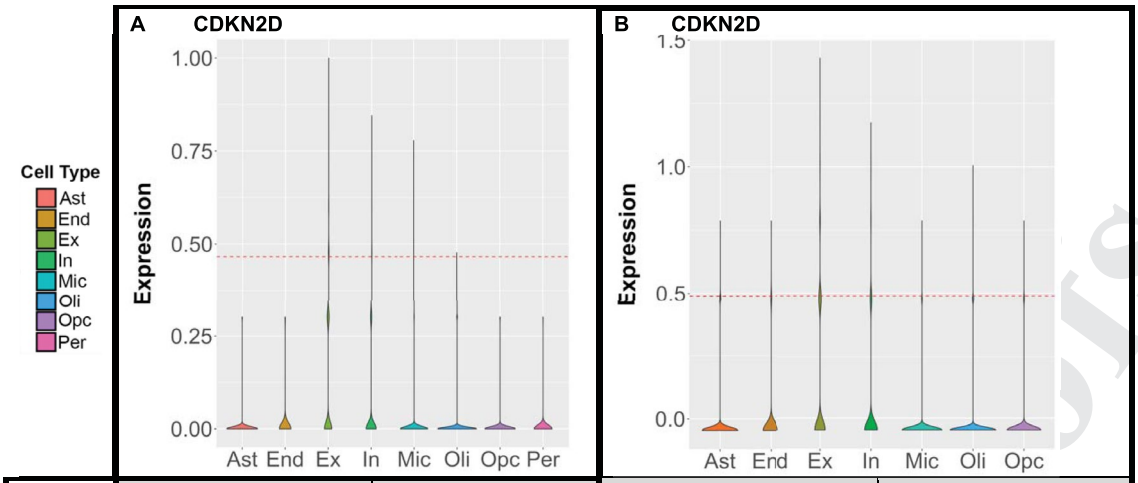

Cell Types	Cell Numbers		log10(p-value)	Cell Numbers		log10(p-value)
	Normal	*CDKN2D*+		Normal	*CDKN2D*+	
Ast	3392	0	0	8713	12	0
End	121	0	-0.02	772	3	-0.01
Ex	32245	2731	-4861	11896	694	-2380
In	9010	186	0	3653	74	-21
Mic	1918	2	0	3744	3	0
Oli	18232	3	0	25355	16	0
Opc	3392	0	0	2919	3	0
Per	121	0	-0.02			
Total	67712	22922	-4861	57052	805	

Extended Data Fig. 6 | Excitatory neurons are the prominent senescent cell types based on CDKN2D in (A) Cohort 1 and (B) Cohort 2. Cell types and counts represented in the senescent cell population using only CDKN2D. The cutoff, statistical tests and abbreviations definitions are the same as in Fig. 1.

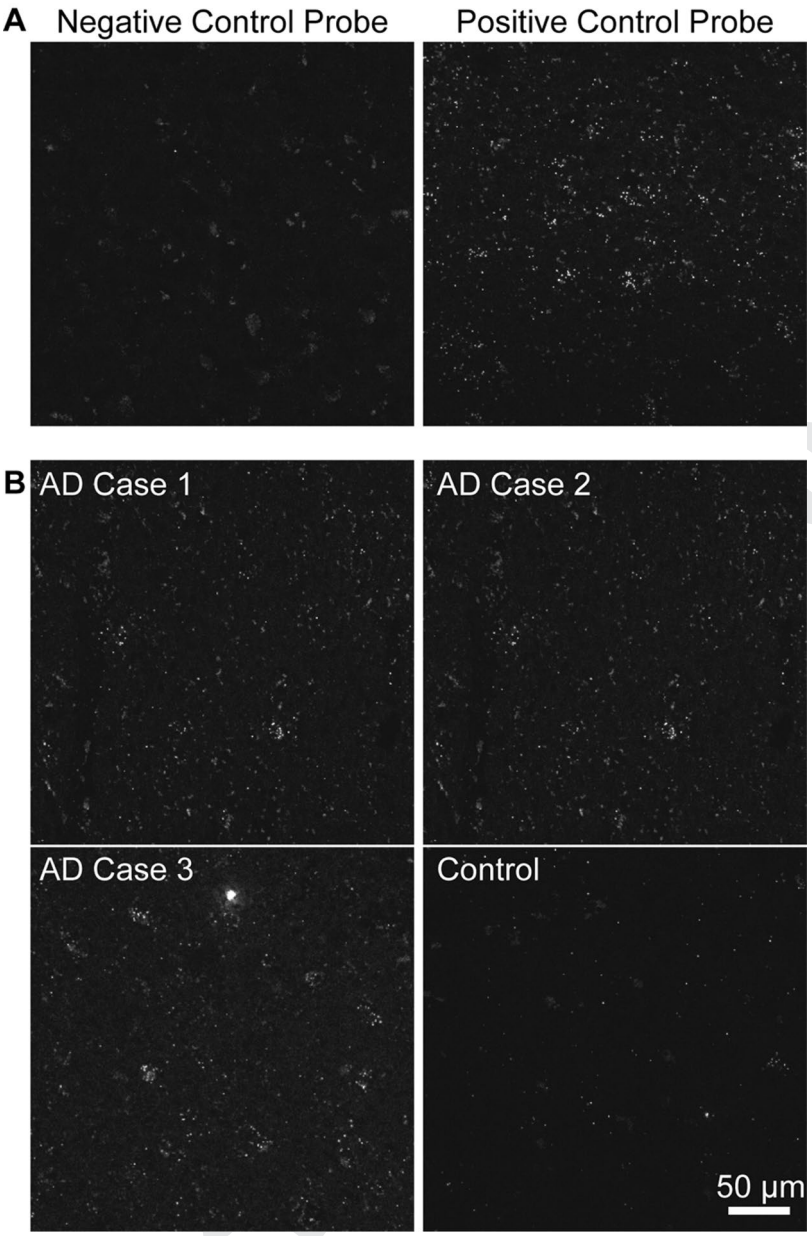

Extended Data Fig. 7 | RNAscope reveals higher CDKN2D expression in postmortem brains from cases with AD than age-matched control brains. A. CDKN2D negative and positive control probe signal. B. CDKN2D RNAscope on three separate AD cases (n = 3) compared to a representative age-matched non-demented control (n = 3) (refer to Supplementary Table 5 for case characteristics. Scale bar 50 µm.

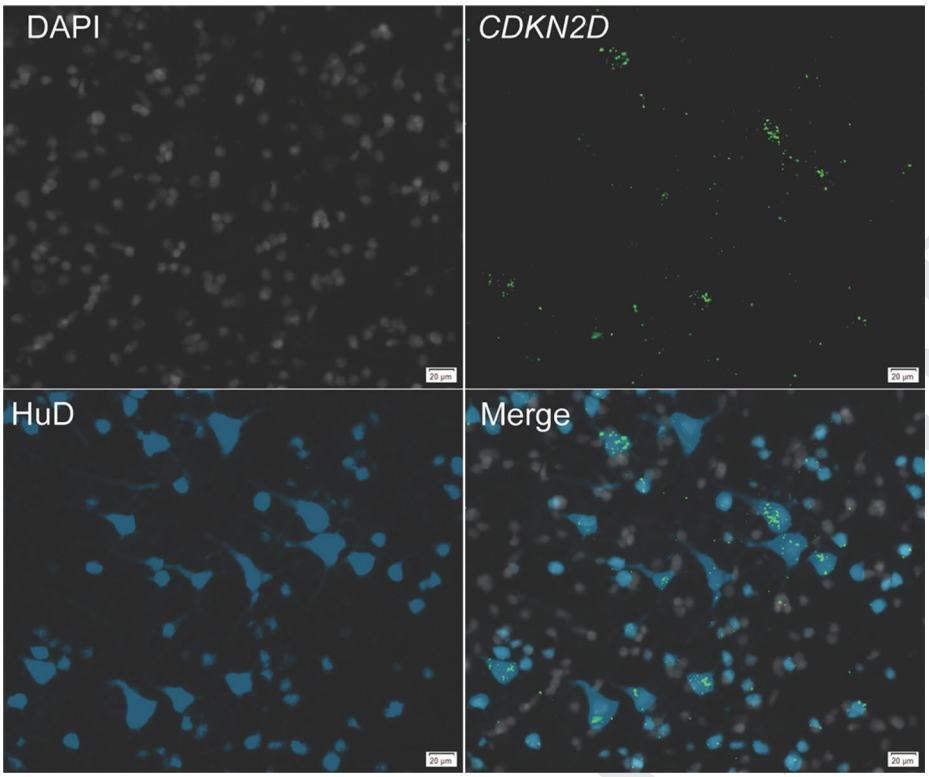

Extended Data Fig. 8 | CDKN2D RNAscope co-localized with neuronal marker, HuD. Postmortem AD tissue was processed for RNAscope with CDKN2D (green) and co-labeled for total nuclei (DAPI, gray) and neurons (HuD, cyan)/ Merged image display strong overlap between CDKN2D and neurons, but not other cell types (that is, blue and green co-localization with infrequent green co-localization in nuclei without HuD staining). Scale bar 10 µm. Representative images from postmortem human brains (n = 3 control and n = 3 AD cases).

QUERY FORM

Nature Aging	
Manuscript ID	**[Art. Id: 142]**
Author	**Shiva Kazempour Dehkordi**

AUTHOR:

The following queries have arisen during the editing of your manuscript. Please answer by making the requisite corrections directly in the e.proofing tool rather than marking them up on the PDF. This will ensure that your corrections are incorporated accurately and that your paper is published as quickly as possible.

Query No.	*Nature of Query*
Q1:	Please ensure that genes are correctly distinguished from gene products: for genes, official gene symbols (e.g., NCBI Gene) for the relevant species should be used and italicized; gene products such as proteins and noncoding RNAs should not be italicized.
Q2:	Your paper has been copy edited. Please review every sentence to ensure that it conveys your intended meaning; if changes are required, please provide further clarification rather than reverting to the original text. Please note that formatting (including hyphenation, Latin words, and any reference citations that might be mistaken for exponents) has been made consistent with our house style.
Q3:	Please check your article carefully, coordinate with any co-authors and enter all final edits clearly in the eproof, remembering to save frequently. Once corrections are submitted, we cannot routinely make further changes to the article.
Q4:	Note that the eproof should be amended in only one browser window at any one time; otherwise changes will be overwritten.
Q5:	Author surnames have been highlighted. Please check these carefully and adjust if the first name or surname is marked up incorrectly. Note that changes here will affect indexing of your article in public repositories such as PubMed. Also, carefully check the spelling and numbering of all author names and affiliations, and the corresponding email address(es).
Q6:	You cannot alter accepted Supplementary Information files except for critical changes to scientific content. If you do resupply any files, please also provide a brief (but complete) list of changes. If these are not considered scientific changes, any altered Supplementary files will not be used, only the originally accepted version will be published.
Q7:	If applicable, please ensure that any accession codes and datasets whose DOIs or other identifiers are mentioned in the paper are scheduled for public release as soon as possible, we recommend within a few days of submitting your proof, and update the database record with publication details from this article once available.
Q8:	Please add individual descriptions to the caption to Fig. 1 to clarify the difference between panels a–h. Please also ensure each panel is described in order.
Q9:	Please give more explanation for the number "77" in the sentence beginning "Similarly, in the embryonic dataset,..."
Q10:	Please add individual descriptions to the caption to Fig. 2 to clarify the difference between panels a and b and d and e.

QUERY FORM

Nature Aging	
Manuscript ID	**[Art. Id: 142]**
Author	**Shiva Kazempour Dehkordi**

AUTHOR:

The following queries have arisen during the editing of your manuscript. Please answer by making the requisite corrections directly in the e.proofing tool rather than marking them up on the PDF. This will ensure that your corrections are incorporated accurately and that your paper is published as quickly as possible.

Query No.	*Nature of Query*
Q11:	Please add individual descriptions to the caption to Fig. 3 to clarify the difference between panels a–f.
Q12:	Please add individual descriptions to the caption to Fig. 4 to clarify the difference between panels a–u and ensure that each panel is described in order.
Q13:	Please note, we reserve 'significant' and its derivatives for statistical significance. Please reword where this is notthe intended meaning (for example to important, notable, substantial); there is one instances throughout yourtext.
Q14:	Please check that all funders have been appropriately acknowledged and that all grant numbers are correct.
Q15:	If applicable, please ensure accession codes are scheduled for release on or before this article's scheduled publication date, and update the database record with publication details from this article once available.
Q16:	Please check that the Competing Interests declaration is correct as stated. If you declare competing interests, please check the full text of the declaration for accuracy and completeness.
Q17:	If ref. 35,52 (preprint) has now been published in final peer-reviewed form, please update the reference details if appropriate.
Q18:	If refs. 35 and 52 (preprints) have now been published in final peer-reviewed form, please update the reference details if appropriate and add url.

nature research

Corresponding author(s): Miranda Orr
Habil Zare

Last updated by author(s): Oct 5, 2021

Reporting Summary

Nature Research wishes to improve the reproducibility of the work that we publish. This form provides structure for consistency and transparency in reporting. For further information on Nature Research policies, see our Editorial Policies and the Editorial Policy Checklist.

Statistics

For all statistical analyses, confirm that the following items are present in the figure legend, table legend, main text, or Methods section.

n/a	Confirmed
☐	☒ The exact sample size (*n*) for each experimental group/condition, given as a discrete number and unit of measurement
☒	☐ A statement on whether measurements were taken from distinct samples or whether the same sample was measured repeatedly
☐	☒ The statistical test(s) used AND whether they are one- or two-sided *Only common tests should be described solely by name; describe more complex techniques in the Methods section.*
☒	☐ A description of all covariates tested
☐	☒ A description of any assumptions or corrections, such as tests of normality and adjustment for multiple comparisons
☐	☒ A full description of the statistical parameters including central tendency (e.g. means) or other basic estimates (e.g. regression coefficient) AND variation (e.g. standard deviation) or associated estimates of uncertainty (e.g. confidence intervals)
☐	☒ For null hypothesis testing, the test statistic (e.g. *F*, *t*, *r*) with confidence intervals, effect sizes, degrees of freedom and *P* value noted *Give P values as exact values whenever suitable.*
☒	☐ For Bayesian analysis, information on the choice of priors and Markov chain Monte Carlo settings
☒	☐ For hierarchical and complex designs, identification of the appropriate level for tests and full reporting of outcomes
☐	☒ Estimates of effect sizes (e.g. Cohen's *d*, Pearson's *r*), indicating how they were calculated

Our web collection on statistics for biologists contains articles on many of the points above.

Software and code

Policy information about availability of computer code

Data collection	We used the synapser (https://r-docs.synapse.org/articles/synapser.html) R package (Version 0.6.61) and custom R scripts (Version 3.6.1) to download the cohort 1 and 2 sn-RNA-Seq datasets from Synapse.
Data analysis	Our R scripts, which are available as supplementary material, can be used to fully reproduce our results. Our code is also publicly available in a Bitbucket repository at https://bitbucket.org/habilzare/alzheimer/src/master/code/senescence/Shiva/.

For manuscripts utilizing custom algorithms or software that are central to the research but not yet described in published literature, software must be made available to editors and reviewers. We strongly encourage code deposition in a community repository (e.g. GitHub). See the Nature Research guidelines for submitting code & software for further information.

Data

Policy information about availability of data

All manuscripts must include a data availability statement. This statement should provide the following information, where applicable:

- Accession codes, unique identifiers, or web links for publicly available datasets
- A list of figures that have associated raw data
- A description of any restrictions on data availability

The sn-RNA-Seq data that were analyzed in this study are available from www.synapse.org with synapse IDs: syn18485175 and syn21126462 for cohorts 1 and 2, respectively. Accessing these data requires submitting a Data Use Certificate through AMP-AD website. Please refer AMP-AD website and the PI of the research group who generated each dataset for details on reasons for controlled access, precise conditions of access, a time frame for response to requests and details of any restrictions imposed on data use via data use agreements. We, as the authors of the current data, did NOT generate those data and do not have any control on these matters.

The scRNA-Seq data from embryonic cortex and the scRNA-Seq data from entorhinal cortex are also available from Gene Expression Omnibus (GEO) with accession numbers GSE103723 and GSE138852. Clinical data were available in the corresponding publications cited in the paper.

Field-specific reporting

Please select the one below that is the best fit for your research. If you are not sure, read the appropriate sections before making your selection.

☒ Life sciences ☐ Behavioural & social sciences ☐ Ecological, evolutionary & environmental sciences

For a reference copy of the document with all sections, see nature.com/documents/nr-reporting-summary-flat.pdf

Life sciences study design

All studies must disclose on these points even when the disclosure is negative.

Sample size	No sample size calculation was performed. We used all datasets that were previously generated in other studies and were available to us.
Data exclusions	Four subjects (i.e, ROS1, ROS23, ROS37, and ROS38) were excluded from the validation cohort 2 because they were included in the training cohort 1 dataset.
Replication	We used the same eigengenes that were calculated from cohort 1 to repeat the analysis on cohort 2, embryonic control and the Grubman scRna-Seq dataset. As in cohort 1, the excitatory neurons were also identified as the prominent senescent cell type in CSP and SIP in cohort 2. This was not true for SRP. One reason for this discrepancy might be that unlike cohort 1, the number of cells labeled as oligodendrocytes in cohort 2 is twice the excitatory cell type. All attempts at replication were successful. Our measures included using multiple bioinformatic approaches on several datasets generated by independent laboratories; reproducing histology experiments using postmortem human brains derived from separate brain biorepositories across three laboratories located in two separate institutions. Specifically, (i) applying our eigengenes to Cohort 2 reproduced findings as in Cohort 1; (ii) creating eigengenes from publicly available senescence gene lists [e.g., CellAge, Gene Ontology (GO), and Kyoto Encyclopedia of Genes and Genomes (KEGG) databases] validated our eigengene results across both Cohorts; (iii) applying a third approach, cell clustering using the Seurat pipeline, further reinforced our findings by confirming the initial eigengene results; (iv) CDKN2D RNAscope confirmed elevated expression in AD brains to validate the bioinformatic results; (v) p19 immunohistochemistry confirmed the CDKN2D RNAscope data using antibodies from two separate vendors (Abcam and Sigma); and (vi) p19 immunofluorescence reproduced the findings predicted by the eigengenes that was confirmed by RNAscope and validated by immunohistochemistry; (vii) histology was performed by three separate laboratories located in separate institutions.
Randomization	We were not working with experimental groups in this study. Clusters of different cell types were previously identified in Mathys and Zhou papers.
Blinding	Blinding was used for histological analyses. Specifically, immunohistochemistry color images were manually scored by a technician blinded to cases. Total cells and p19 positive cells were counted on a minimum of 2 representative images. The images were pre-selected by a neuropathologist to ensure similar brain regions were represented across cases. To determine co-localization of p19, confocal images were analyzed by a technician blinded to cases.

Reporting for specific materials, systems and methods

We require information from authors about some types of materials, experimental systems and methods used in many studies. Here, indicate whether each material, system or method listed is relevant to your study. If you are not sure if a list item applies to your research, read the appropriate section before selecting a response.

Materials & experimental systems

n/a	Involved in the study
☐	☒ Antibodies
☒	☐ Eukaryotic cell lines
☒	☐ Palaeontology and archaeology
☒	☐ Animals and other organisms
☒	☐ Human research participants
☒	☐ Clinical data
☒	☐ Dual use research of concern

Methods

n/a	Involved in the study
☒	☐ ChIP-seq
☒	☐ Flow cytometry
☒	☐ MRI-based neuroimaging

Antibodies

Antibodies used	Mouse monoclonal anti-human phospho-Tau (Ser202,Thr205) clone AT8, 1:100, (ThermoFisher Scientific, MN1020); mouse polyclonal anti-MAP2, 1:100, (PA5-17646, Invitrogen); Rabbit polyclonal anti-human P19 INK4d, 1:100, (Abcam, ab262871 and Sigma, HPA043546); mouse polyclonal anti-Lamin B1, 1:500, (ThermoFisher Scientific, clone 10H34L18, cat no. 702972); mouse monoclonal anti-HuD, 1:500 (E-1; cat no. sc-28299). Secondary antibodies: Goat anti-Rabbit IgG (H+L) Highly Cross-Adsorbed Secondary Antibody, Alexa Fluor Plus 647, 1:1500; (Invitrogen, Catalog # A32733); Goat anti-Mouse IgG (H+L) Highly Cross-Adsorbed Secondary Antibody, Alexa Fluor Plus 555, 1:1500 (Invitrogen, Catalog # A32727).

Validation	All the primary antibodies have been validated by either the manufacturer or other uses in the published studies which could be found on the manufacturer's website. Examples include: AT8 has received an “Advanced Verification” badge by Invitrogen as it has been verified by Cell treatment to ensure that the antibody binds to the antigen stated. We have validated AT8 using tau over-expression and tau knockout samples (Orr et al 2012 PlosOne, PMC3377636). Similarly, anti-Map2 has received the same badge by Invitrogen; it was verified by Relative expression levels in vitro across several cell lines and brain developmental changes by our group (Orr et al 2016, Front Neurosci; PMC5099538). Anti-P19 has received the Abcam “Abpromise” which guarantees product applications & species that have been tested in their labs, by their suppliers, or by selected trusted collaborators. Additionally, this is a Prestige Antibody® all of which undergo in-depth validation as well as characterization using the immense amount of supporting data from the Human Protein Atlas project. The low cross reactivity for Prestige Antibodies® to other proteins is the result of careful selection of antigen regions, affinity purification, and are validated and characterized in each application that the antibody has been demonstrated for use. Each antibody is characterized on a lot-to-lot basis with application-specific validation that includes IHC, IF, WB, and or protein array assays. The anti-Lamin B1 antibody was verified by knockdown to ensure that the antibody binds to the antigen stated. From the vendor web site: Antibody specificity was demonstrated by siRNA mediated knockdown of the target protein. HeLa cells were transfected with Lamin B1 siRNA and a decrease in signal intensity was observed in Western blot application using Anti-Lamin B1 Recombinant Rabbit Monoclonal Antibody cat# 70297). HuD (E-1) is a mouse monoclonal antibody raised against amino acids 1-300 of HuD of human origin.